

Serveur Académique Lausannois SERVAL serval.unil.ch

Author Manuscript

Faculty of Biology and Medicine Publication

This paper has been peer-reviewed but does not include the final publisher proof-corrections or journal pagination.

Published in final edited form as:

Title: Multispectral fluorine-19 MRI enables longitudinal and noninvasive monitoring of tumor-associated macrophages.

Authors: Croci D, Santalla Méndez R, Temme S, Soukup K, Fournier N, Zomer A, Colotti R, Wischnewski V, Flögel U, van Heeswijk RB, Joyce JA

Journal: Science translational medicine

Year: 2022 Oct 19

Issue: 14

Volume: 667

Pages: eabo2952

DOI: [10.1126/scitranslmed.abo2952](https://doi.org/10.1126/scitranslmed.abo2952)

In the absence of a copyright statement, users should assume that standard copyright protection applies, unless the article contains an explicit statement to the contrary. In case of doubt, contact the journal publisher to verify the copyright status of an article.

Title:

Multispectral fluorine-19 MRI enables longitudinal and noninvasive monitoring of tumor-associated macrophages

Authors:

Davide Croci ^{1,2,3}, Rui Santalla Méndez ^{1,2,3}, Sebastian Temme ^{4,5}, Klara Soukup ^{1,2,3}, Nadine Fournier ^{3,6}, Aniek Zomer ^{1,2,3}, Roberto Colotti ⁷, Vladimir Wischnewski ^{1,2,3}, Ulrich Flögel ^{5,8}, Ruud B. van Heeswijk ^{9,†} and Johanna A. Joyce ^{1,2,3 †,*}

Affiliations:

¹ Department of Oncology, University of Lausanne; Lausanne 1011, Switzerland.

² Ludwig Institute for Cancer Research, University of Lausanne; Lausanne 1011, Switzerland.

³ Agora Cancer Research Center, Lausanne 1011, Switzerland.

⁴ Department of Anesthesiology, Universitätsklinikum Düsseldorf, Heinrich-Heine-Universität; Düsseldorf, Germany.

⁵ Experimental Cardiovascular Imaging, Universitätsklinikum Düsseldorf, Heinrich-Heine-Universität; Düsseldorf, Germany.

⁶ Bioinformatics Core Facility, SIB Swiss Institute of Bioinformatics; Lausanne, Switzerland.

⁷ In Vivo Imaging Facility (IVIF), Department of Research and Training, Lausanne University Hospital and University of Lausanne; Lausanne 1011, Switzerland.

⁸ Institute for Molecular Cardiology, Universitätsklinikum Düsseldorf, Heinrich-Heine-Universität Düsseldorf; Düsseldorf, Germany.

⁹ Department of Radiology, Lausanne University Hospital and University of Lausanne; Lausanne 1011, Switzerland.

† Co-senior authors

* Corresponding author. Email: johanna.joyce@unil.ch

One Sentence Summary: We imaged tumor-associated microglia and macrophages in the brain tumor microenvironment with integrated cellular, spatial and temporal resolution using multispectral fluorine-19 MRI.

Abstract:

High-grade gliomas, the most common and aggressive primary brain tumors, are characterized by a complex tumor microenvironment (TME). Among the immune cells infiltrating the glioma TME, tumor-associated microglia and macrophages (TAMs) constitute the major compartment. In patients, increased TAM abundance is associated with more aggressive disease. Importantly, alterations in TAM phenotypes and functions have been reported in preclinical models during tumor development and following therapeutic interventions, including radiotherapy (RT) and molecular targeted therapies. These findings indicate that it is crucial to evaluate TAM abundance and dynamics over time. Current techniques to quantify TAMs in patients rely mainly on histological staining of tumor biopsies. While informative, these techniques require an invasive procedure to harvest the tissue sample and typically only result in a snapshot of a small region at a single point in time. Fluorine isotope 19 MRI (^{19}F MRI) represents a powerful means to non-invasively and longitudinally monitor myeloid cells in pathological conditions by injecting perfluorocarbon-containing nanoparticles (PFC-NP). In this study, we demonstrated the feasibility and power of ^{19}F MRI in preclinical models of gliomagenesis, breast-to-brain metastasis, and breast cancer, and showed that the major cellular source of ^{19}F signal consists of TAMs. Moreover, multispectral ^{19}F MRI with two different PFC-NP allowed us to identify spatially- and temporally-distinct TAM niches in RT-recurrent murine gliomas. Together, we have imaged TAMs non-invasively and longitudinally with a powerful integrated cellular, spatial and temporal resolution, while revealing important biological insights into the critical functions of TAMs, including in disease recurrence.

Main Text:

INTRODUCTION

The brain tumor microenvironment (TME) is composed of malignant cancer cells, tissue-resident and peripherally-recruited immune cells, stromal cells, astrocytes and neurons, along with non-cellular components, that collectively orchestrate tumor development and modulate the response to anti-cancer treatments (1, 2). The precise composition and phenotypes of immune cells in the brain TME is dictated by several parameters, including the intracranial or extracranial origin of the tumor, the genetic drivers of the cancer, and the type of therapeutic intervention (3-5).

The most aggressive primary brain tumors in adults are high-grade gliomas, also termed glioblastoma (6). Despite treatment with standard-of-care therapy, which includes surgical resection, radiotherapy (RT) and chemotherapy with the alkylating agent temozolomide (TMZ), median survival remains just 14 months following diagnosis, and the five-year survival is <5% (7). Recent comprehensive analyses of the immune cell composition of diverse brain malignancies in patients, including low- and high-grade gliomas, and brain metastases originating from different primary cancers, revealed disease-specific alterations in both immune cell abundance and functions (3, 4). The immune microenvironment of high-grade gliomas was found to be predominantly populated by tumor-associated macrophages (TAMs) comprising brain-resident microglia (MG) and monocyte-derived macrophages (MDMs) that were recruited from the peripheral circulation (3, 4). Standard-of-care therapies, including RT and TMZ, have been shown to directly alter the TME composition, with pronounced effects on myeloid cells in particular (5, 8). Indeed, time course analyses, incorporating several fixed timepoints, showed that the relative abundance and phenotypes of MG and MDMs changed in response to RT in multiple genetically-distinct murine glioma models (5). Importantly, combining RT with therapeutic targeting of TAMs via colony stimulating factor-1 receptor (CSF-1R) inhibition to 're-educate' these cells, or by depletion of MDMs, resulted in a significantly prolonged survival of the animals (5). CSF-1R inhibition has been shown to be a promising and translationally relevant approach in several preclinical studies using models of diverse brain cancers (5, 9-14), and clinical trials with a potent CSF-1R inhibitor (BLZ945) are ongoing in patients with advanced cancer, including gliomas (NCT02829723) (15). The evolving TME was also recently assessed in response to TMZ chemotherapy, which revealed specific myeloid cell dynamics during tumor progression and upon treatment in distinct models of mesenchymal and proneural glioma (8).

Dynamic monitoring of the cells of the brain TME is therefore crucial to fully understand the disease biology and response to treatment. While TAMs can be analyzed using a multitude of experimental techniques in preclinical models, TAM quantification in patients currently relies mainly on histological staining of tumor biopsies. This approach has several limitations, including the fact that biopsies only represent a small portion of the entire tumor and thus do not necessarily capture the full tissue heterogeneity. Moreover, surgical access to the brain is challenging, which does not facilitate frequent and repeated sampling to follow cellular dynamics over time. It is therefore essential to develop new technological strategies that will enable the non-invasive and longitudinal monitoring of multiple aspects of the disease, including changes in the TME composition.

Magnetic resonance imaging (MRI) is a widely used and indispensable imaging modality in neuro-oncology, where it enables key decision-making steps - including tumor diagnosis, a precise guidance for planning surgery and targeted RT, and also for monitoring the subsequent response to treatment (16). Historically, MR images have been primarily used for a qualitative and objective assessment of the tumor by clinicians. However, recent neuroimaging advances have contributed to the development of quantitative and molecular MRI techniques (17-19), which have the potential to transform the interpretation and application of imaging results into routine clinical practice. Nonetheless, research into fully quantitative MRI-based biomarkers of glioma is still very much an ongoing endeavor. The major challenges include the technical, biological and clinical validation of such biomarkers, in order to implement robust imaging methods that will enable the acquisition of multiparametric information, including TME-centered data (16).

The clinical application of macrophage imaging requires safe and biocompatible targeting agents and an accurate and precise interpretation of the resulting signal. Several MRI-based non-invasive molecular imaging techniques fulfill these conditions for a potentially powerful strategy to visualize myeloid cells (20, 21). Among these, isotope fluorine-19 MRI (^{19}F MRI) takes advantage of perfluorocarbon-containing nanoparticles (PFC-NP), such as perfluoro-crown-ether (PFCE) or perfluoro-tert-butylcyclohexane (PFTBH) (22, 23), and has been mostly used for non-neurological applications to date (24, 25). PFCs are biologically inert organic compounds that are highly enriched in the stable isotope fluorine-19 (^{19}F). The ^{19}F isotope is not naturally present in the body, and the ^{19}F signal is completely independent from the hydrogen signal normally used for routine MRI (^1H MRI). Thus, ^{19}F MRI enables a precise signal detection and quantification

upon the injection of PFC-NP. Myeloid cells generally have a high capacity for phagocytosis, and their uptake of PFC-NP has been used as a readout for inflammation-related processes (24-27). Due to the critical role of TAMs in regulating tumor biology and influencing therapeutic response, we decided to investigate ^{19}F MRI as a strategy to non-invasively longitudinally monitor TAMs *in vivo* in experimental mouse models of gliomagenesis, breast-to-brain metastasis, and primary breast cancer. In this study, we report the successful tracking of different TAM populations with integrated cellular, spatial and temporal resolution, which has allowed us to reveal novel biological insights into the dynamic evolution of the TME. This study also serves to highlight the potential of *in vivo* ^{19}F MRI to ultimately complement, or perhaps even replace, the existing histological-based assessment of TAMs in patient samples.

RESULTS

Multiparametric magnetic resonance imaging (MRI) reveals a tumor-restricted accumulation of perfluoro-crown-ether-containing nanoparticles (PFCE-NP) in preclinical models of multiple cancers.

We began by assessing whether multiparametric ^1H and ^{19}F MRI can be used in conjunction for molecular imaging of several preclinical cancer models. We first analyzed a genetically-engineered mouse model (GEMM) of gliomagenesis, in which nestin-positive neural progenitor cells overexpress the oncogenic platelet-derived growth factor- β (PDGF- β) by taking advantage of the transgenic RCAS-tva delivery strategy (28). High-grade gliomas develop in a highly penetrant manner when this model is crossed into an *Ink4a/Arf* tumor suppressor-deficient background (termed PDG-Ink4a/Arf KO GEMM) (5, 11, 28-30). Tumor-bearing mice were injected with a PFCE-NP emulsion and imaged 48 hours later using a 3T clinical MRI scanner (Prisma, Siemens) equipped for both ^1H and ^{19}F sequential imaging (Fig. 1A). We detected a robust ^{19}F signal and PFCE accumulation inside the gliomas, which were anatomically defined by standard ^1H MRI (Fig. 1B). By contrast, the contralateral healthy brain, as well as the brain of control non-tumor bearing mice, did not show any ^{19}F signal (fig. S1A). Importantly, the measured PFCE concentrations were above the detection limit of PFCE at 3T (fig. S1B). Of note, brain tumors can display diverse anatomical features by ^1H MRI, which may indicate functionally discrete regions (31). We therefore analyzed the extent of the ^{19}F distribution in detail, and found that the proportion of the total tumor volume covered by ^{19}F signal varied considerably and showed distinct patterns in different animals (Fig. 1C and fig. S1C). We also observed PFCE accumulation in the liver (Fig. 1A and fig. S1A), in agreement with a previous description of its function in PFCE uptake and excretion (22). Therefore, the ability to assess whole-body ^{19}F distribution *in vivo* in this manner represents an important advance over the recently reported static *ex vivo* ^{19}F MRI of a glioma model that was generated by intracranial injection of cancer cells (32).

We next asked whether this imaging strategy could also be applied to other brain cancer models, and evaluated the ^1H - ^{19}F MRI pipeline in a breast-to-brain metastasis (BrM) mouse model, termed PyMT-BrM3. We generated the PyMT-BrM3 cell line from the sequential *in vivo* selection (3 rounds) of a metastatic cell line that was originally derived from the MMTV-PyMT mammary tumor model (BL/6 background). Intracardiac injection of PyMT-BrM3 cells in BL/6 mice leads to cancer cell circulation in the blood, extravasation, seeding and outgrowth of multiple lesions throughout

the brain parenchyma. By comparison with PDG-Ink4a/Arf KO gliomas, the ^{19}F coverage of the metastatic lesions was lower, as reflected by the lower PFCE concentration and amount in the PyMT-BrM3 model (fig. S1, D, E and F). Nonetheless, in both gliomas and brain metastases there was a positive correlation between the total amount of PFCE and tumor volume as determined by ^1H MRI (Fig. 1D and fig. S1F). Primary breast tumor models have been reported to display a ^{19}F signal upon injection of PFC agents (33, 34). We therefore investigated if extracranial tumors might accumulate more PFCE-NP, by injecting the PyMT-BrM3 cell line orthotopically in the mammary fat pad (termed 'primary breast tumor' model). Upon ^{19}F MR imaging, we indeed found a higher PFCE accumulation than in the corresponding brain metastatic lesions (fig. S1G), indicating that properties of the brain or the brain TME might impact the PFCE-NP uptake. Together, these results demonstrate that multiparametric MRI is technically feasible *in vivo* in different preclinical cancer models and can be used to reveal valuable molecular information in addition to conventional ^1H MRI. The heterogenous ^{19}F pattern observed in the glioma and BrM models, and the higher total amount of PFCE in larger brain tumors, as well as in extracranial tumors, suggest that a specific cellular composition as well as functionally distinct regions within the tumor could potentially underlie the ^{19}F signal distribution, which we subsequently investigated in detail.

We first asked whether the ^{19}F signal-to-noise ratio (SNR) correlated with the presence of any specific cell population, which was assessed by flow cytometry (FCM) analysis of the cellular composition of the tumor. Interestingly, we found that myeloid cell abundance in general, and TAMs specifically, correlated positively with the ^{19}F SNR (Fig. 1E and fig. S1H), which was opposite to the abundance of non-immune cells (fig. S1I). To determine if there was a direct dependency of the ^{19}F SNR with macrophage abundance, we measured the ^{19}F signal in primary breast tumors which were treated with BLZ945, an anti-CSF1R inhibitor which has previously been shown to deplete macrophages in similar models (35, 36). Indeed, we found a lower ^{19}F SNR following *in vivo* treatment of tumor-bearing mice (fig. S1J). Together, these results indicate that the ^{19}F signal represents a direct readout of macrophage abundance, and we subsequently investigated the exact cellular source and accumulation of the PFCE-NP.

PFCE-NP accumulate in tumor-associated microglia and macrophages in gliomas enabling their specific imaging by ¹⁹F MRI.

¹⁹F MRI has been utilized in different models of inflammatory disease, where myeloid cells at the site of inflammation have been shown to take up injected PFC-NP (25, 34, 37). However, this powerful imaging approach has not yet been widely applied to assess the dynamics of cancer-associated inflammation *in vivo*. Brain tumor development and progression can result in heterogenous breakdown of the blood-brain barrier (BBB), facilitating the entry of peripheral immune cells, mainly of myeloid origin, which along with the various brain-resident cells contribute to form a complex and diverse brain tumor microenvironment (TME) (1-4). We therefore assessed the exact cellular source of the ¹⁹F signal that we observed in the PDG-Ink4a/Arf KO GEMM. To do so, we injected glioma-bearing mice with fluorescent rhodamine-labelled PFCE-NP (rhodamine-PFCE-NP), allowed the NP to circulate for 24 hours, and analyzed the cellular composition of the tumors by FCM at the end of the experiment. We observed a high abundance of myeloid cells in gliomas *per se* (fig. S2A), as previously described for this mouse model (5, 11, 28-30), and similar to analyses of patient samples (3, 4). In our analysis, specifically investigating the rhodamine-PFCE-NP⁺ cells (Fig. 2A and fig. S2B), we found that myeloid cells accounted for the majority of positive cells by FCM. TAMs, together with a smaller proportion of monocytes, constituted the rhodamine-PFCE-NP⁺ myeloid pool (Fig. 2, B and C). While we also detected rhodamine-PFCE-NP in some non-immune cells by FCM, the median fluorescence intensity (MFI) of rhodamine was substantially higher in both resident MG and recruited MDMs (Fig. 2D), indicating a substantial enrichment of nanoparticles specifically in these cells. Importantly, TAMs have been shown to represent a very heterogenous cellular population (38). We therefore investigated in detail the granularity of the TAM compartment with relation to the rhodamine-PFCE-NP uptake by performing t-distributed stochastic neighbor embedding (tSNE) analysis of the FCM data (Fig. 2E). We identified both MG and MDM populations, defined by differential expression of CD49d and CD45 (29), which were additionally clustered in subpopulations characterized by the differential expression of the major histocompatibility complex II (MHCII), CD11c, CD64 and F4/80. Interestingly, we found that the majority of the MHCII⁺ CD11c⁺ CD64⁻ F4/80⁻ cells were enriched in the rhodamine-PFCE-NP negative fraction, indicating no uptake by this population (fig. S2C). In order to evaluate any extra-cellular deposition or accumulation of the nanoparticles, we also analyzed tissue sections by immunofluorescence (IF) staining with the pan-macrophage marker Iba1 and staining of all cell membranes using the wheat germ agglutinin

(WGA) (Fig. 2F). We observed nanoparticle accumulation within Iba1⁺ macrophages, while no extra-cellular deposition was detected (Fig. 2G). These data corroborated our finding that the ¹⁹F SNR correlated with a high abundance of TAMs in gliomas (Fig. 1E).

We then assessed the proportion of rhodamine-PFCE-NP⁺ cells in a cell type-specific manner (Fig. 2H, and fig. S2, D and E). We found that while myeloid cells represented the major rhodamine-PFCE-NP⁺ population, only a small percentage within the different cell populations accumulated the rhodamine-PFCE-NP. A higher frequency of rhodamine-PFCE-NP⁺ cells was observed in TAMs compared to monocytes (Fig. 2H), and uptake by cells of lymphoid origin or non-immune cells was generally low (fig. S2E). Interestingly, CD31⁺ endothelial cells showed a slightly higher frequency of rhodamine-PFCE-NP⁺ cells compared to other non-immune cells (fig. S2E), which could indicate a role for the vasculature in the distribution of the NP (see following section). Given that the TME composition can change dynamically over time, partly as a consequence of the infiltration of newly-recruited immune cells from the periphery, we also assessed the uptake of rhodamine-PFCE-NP in myeloid cells isolated from the blood and the bone marrow. However, we did not find a significant accumulation of the compound in these tissues (fig. S2F), and thus consider it unlikely that cells recruited *de novo* from outside the brain would substantially impact the ¹⁹F signal in the days following PFCE-NP injection. Together, we were able to identify TAMs as the major cellular contributor to the pool of rhodamine-PFCE-NP⁺ cells, showing both a higher accumulation and MFI signal compared to the other cell types analyzed. Therefore, we conclude that TAMs are the major source of the ¹⁹F signal detected by MRI.

PFCE-NP accumulate in proximity to dysmorphic vessels.

MR imaging revealed a ¹⁹F signal localized to the tumor mass, and not in the contralateral healthy brain, suggesting the presence of an inflammatory microenvironment specifically in the diseased tissue area. Similarly, we did not observe any rhodamine-PFCE-NP uptake in the contralateral tumor-free brain (fig. S2G). While MG isolated from both the tumor and the normal contralateral brain were both capable of uptaking the rhodamine-PFCE-NP *ex vivo* in cell culture (Fig. 2I and fig. S2H), CD45⁺ CD11b⁻ lymphocytes were not (fig. S2I). This indicates that the absence of uptake *in vivo* in the contralateral brain could be related to the nanoparticle distribution, rather than differences in the phenotypes or phagocytic capabilities of the microglia. While the BBB

protects the brain from entry of exogenous substances and pathogens under normal homeostasis, thereby constituting a potential hurdle for PFCE-NP distribution, it can be compromised in brain malignancies (39). Given the small percentage of cells showing accumulation of the rhodamine-PFCE-NP (Fig. 2H and fig. S2E), the absence of uptake in the contralateral brain *in vivo* (Fig. S2G), and the heterogenous ^{19}F signal within the tumor (Fig. 1C), we reasoned that the abnormal nature of the brain tumor vascular network could impact the differences in observed PFCE-NP distribution. To investigate this further, we induced PDG-Ink4a/Arf KO gliomas that were expressing green-fluorescent protein (GFP), thereby enabling precise visualization of the tumor mass, and investigated the distribution pattern of rhodamine-PFCE-NP. To image the vasculature, we injected DyLight649-fluorescent lectin intravenously and allowed it to circulate for 5 minutes before sacrificing the mouse. Interestingly, IF analysis showed that the rhodamine-PFCE-NP⁺ Iba1⁺ cells localized in the vicinity of the vessels (fig. S3, A and B). We therefore investigated whether this accumulation was related to specific morphological properties of the tumor vasculature. In order to retain the 3D structure of the vessels, and as the rhodamine-PFCE-NP signal can be sensitive to degradation post-tissue processing (40), we imaged freshly-cut 425 μm -thick tissue slices *ex vivo* with a 2-photon microscope, immediately after harvesting and slicing of the brain. We observed a heterogenous pattern of NP accumulation, whereby distinct regions within the same tumor showed a differential distribution of the rhodamine signal (Fig. 3A).

We reconstructed the imaged slices using the analysis software *Imaris* (fig. S3C) and first assessed whether the accumulation was similar to the FCM results discussed above. Indeed, we found that only a minor proportion of the rhodamine⁺ foci were also GFP⁺ (indicating tumor cells) (fig. S3D), and similarly, only a small percentage of GFP⁺ cells showed a rhodamine signal (fig. S3E). We then examined how the tumor vasculature might impact the degree of accumulation of the rhodamine-PFCE-NP. Image reconstruction using *Imaris* enabled a multi-parametric analysis of the tumor vessels, including vessel dendrite morphology, orientation and branching (fig. S3F). A principal component analysis of all vascular morphological parameters showed the independent clustering of rhodamine^{HIGH} areas (with respect to the healthy brain parenchyma) (Fig. 3B). Together, these analyses revealed a heterogenous vascular morphology within the tumors, ranging from “healthy brain-like” vessels to a completely dysmorphic vasculature, which precisely correlated with the amount of rhodamine-PFCE-NP accumulation (Fig. 3B).

We then sought to longitudinally assess the kinetics of rhodamine-PFCE-NP distribution by taking advantage of a recently established intravital microscopy (IVM)- MRI pipeline in living animals (41). We induced GFP⁺ tumors in the PDG-Ink4a/Arf KO GEMM, where a cranial imaging window (CIW) was surgically implanted in the skull at the site of tumor induction. Following tumor detection by conventional ¹H MRI, mice were imaged by 2-photon microscopy enabling longitudinal live imaging within the GFP⁺ tumor area precisely below the CIW (Fig. 3C). Immediately after injection of the rhodamine-PFCE-NP, we analyzed the dynamics of the rhodamine signal inside the blood vessels, which were highlighted by the circulating fluorescent nanoparticles (Fig. 3D and fig. S3G). We found that the rhodamine signal was almost completely cleared from the blood circulation 6 hours after NP injection. In line with our results above showing a heterogenous pattern of rhodamine^{LOW/HIGH} regions, we were able to detect a clear signal *in vivo* directly below the CIW in 2 out of 11 mice that were imaged (Fig. 3D, Supplementary Videos 1, 2 and 3).

Given the higher NP uptake in regions with dysmorphic vessels, we next sought to address whether the NP were subsequently distributed effectively from the circulation into the tumor mass. We thus analyzed the distance of the rhodamine⁺ foci to the vessels (and GFP⁺ cancer cells to the vessels) in tumor-bearing brain slices and found that NP accumulated in proximity to the vasculature (Fig. 3E). GFP⁺ cancer cells with a detectable rhodamine signal were also closer to the vessels compared to rhodamine-negative cancer cells (fig. S3H). Since the positioning of TAMs relative to the vasculature potentially affects their phenotype and oxidative metabolism (42), we asked whether the specific distribution pattern of rhodamine-PFCE-NP⁺ TAMs could reflect a precise subpopulation. We therefore used fluorescence-activated single cell sorting (FACS) to collect rhodamine-PFCE-NP⁺ and rhodamine-PFCE-NP⁻ TAMs respectively and performed RNA sequencing (RNA-seq) (fig. S4A). TAMs were gated as CD45⁺ CD11b⁺ Ly6G⁻ Ly6C⁻ cells, in order to obtain a broad overview of the population-based phenotypes, rather than focusing too narrowly on isolating each of the different subpopulations identified by FCM (Fig. 2E). Interestingly, in line with their perivascular location, gene-set enrichment analysis (GSEA) revealed a higher oxidative phosphorylation activity in the rhodamine-PFCE-NP⁺ population (Fig. 4A), consistent with an altered metabolism. Moreover, GSEA network analysis showed an enrichment of several mitochondrial components (Fig. 4B), and central enzymes of the tricarboxylic acid (TCA) cycle, including *Dlat*, *Idh1*, and *Idh2* (Fig. 4C). To validate the RNA-seq results, we stained glioma tissue sections by IF for the macrophage marker CD68 and the metabolic enzyme IDH2 (Fig. 4D). We

identified two TAM subpopulations: a IDH2⁺ subset in proximity to CD31⁺ endothelial cells, and a larger proportion of IDH2⁻ TAMs which were more distant from the vessels (Fig. 4E and fig. S4B). Together, these results indicate that rhodamine-PFCE-NP⁺ TAMs are characterized by an oxidative metabolic signature, including high *Idh2* expression, and are localized within perivascular niches.

¹⁹F MRI allows the non-invasive and longitudinal monitoring of TAMs in gliomas following radiotherapy (RT).

We next asked whether ¹⁹F MRI could be used to monitor changes in the TME following therapeutic intervention in a non-invasive and longitudinal manner. RT is part of the standard of care therapy for glioma patients (7), and has been shown to alter the composition of the glioma TME (5, 38). Notably, time course analyses of fixed timepoints previously revealed that the overall abundance and phenotypes of TAMs were substantially impacted by RT, in addition to alterations in the relative proportions of recruited MDMs versus brain-resident MG (5). While PFCE-NP uptake occurred in a subset of TAMs at baseline, as shown in our analyses above, we sought to address whether this population would be indicative and representative of general TAM dynamics following RT. We therefore first injected glioma-bearing mice with a single dose of PFCE-NP, which has been previously reported to be slowly cleared from the liver (22), to specifically track the dynamics of the initial TAM pool only. Mice were then imaged by ¹H and ¹⁹F MRI, to determine the baseline PFCE concentration and tumor volume before RT, and subsequently imaged weekly until tumor recurrence (Fig. 5A).

Single dose RT treatment led to an initial tumor regression, followed by a quiescent phase, and eventually all tumors relapsed (Fig. 5B). First, we analyzed TAM dynamics by IF after RT treatment (single dose of 10 Gy) (Fig. 5C). Consistent with previous reports employing fractionated RT (5), we found a transient increase in the abundance of all TAMs following single dose RT, with a peak at 7 days after treatment (Fig. 5C). We then quantified the PFCE concentration over time, in a separate cohort, and found a significant increase 7 days after RT (Fig. 5D), consistent with the observed abundance of TAMs by IF staining (Fig. 5C). Normalization of the tumor PFCE concentration to the liver PFCE concentration, as a measure of potential compound clearing, confirmed the increase following RT (fig. S5A). The total PFCE amount normalized to the ¹H tumor volume also increased after treatment (fig. S5B). Importantly,

the PFCE concentration was stable in the liver over the full time course, indicating a very slow clearing of PFCE (fig. S5, C and D), consistent with previous reports (22). Moreover, we did not observe changes in the amount of PFCE inside the tumor (fig. S5E), indicating a cellular labelling only after compound administration, in line with our results from FCM and IVM that showed no peripheral PFCE-NP uptake and a rapid clearance from the bloodstream (fig. S2F and fig. S3G). Overall, these results demonstrated that ^{19}F MRI can be used to track the initial TAM dynamics at 7 days post-RT treatment.

We also investigated whether the changes in ^{19}F signal over the full trial length could be indicative of the long-term TAM dynamics that we observed by IF staining at different timepoints (Fig. 5C), where overall TAM abundance returns to the baseline level at tumor recurrence. First, we addressed if the tumor PFCE concentration returned to the initial levels (fig. S5F). We found that the tumor PFCE concentration indeed tended to decrease in the subset of mice that could be imaged until 28 days post-RT (not all treated animals survived to this timepoint), although the reduction was not statistically significant (fig. S5F). Importantly, one needs to additionally account for a decreased total PFCE amount in the tumor, probably related to local clearing, that consequently affects the PFCE concentration (fig. S5G). Together, these results showed that after an initial precise monitoring of the RT-mediated TAM increase, long-term ^{19}F MRI did not enable a comprehensive assessment of TAM dynamics over the full time course of the trial, and we therefore sought to use additional approaches to address this further.

Multispectral ^{19}F MRI identifies spatial- and temporally-distinct cellular populations in RT recurrent tumors.

Previous findings in the context of fractionated RT revealed a shift in the MDM:MG ratio in recurrent tumors by FCM analysis (5). However, the spatial distribution of these cell populations has not been investigated to date. To evaluate TAM changes during the complete duration of the trial, we began by analyzing the ^{19}F signal volume at different time points after RT (Fig. 6, A and B). At recurrence, we observed that the ^{19}F signal volume remained constant (Fig. 6A), in contrast to the ^1H MRI signal increase that reflected the growth of recurrent tumors (Fig. 5B). Topographical examination of the ^{19}F signal showed that it was restricted to a specific region of the recurrent glioma, which could potentially reflect spatially distinct TAM clusters at recurrence (Fig. 6B). We therefore analyzed the composition of the major TAM populations in untreated and

RT-recurrent PDG-Ink4a/Arf KO gliomas in Cx3cr1:CreERT2-IRES-YFP;Rosa26:lsITdTomato mice that allow one to distinguish MG (YFP⁺/tdTomato⁺) and MDMs (YFP⁺/tdTomato⁻) (termed CX3CR1 lineage-tracing model) (29, 43), and by IF staining of the pan-macrophage marker Iba1 and the MG-specific marker P2RY12 (Fig. 6C and fig. S6A). We observed a shift in these TAM populations between untreated and RT-recurrent tumors, consistent with previous FCM findings (5). While MG are the predominant TAM population in untreated gliomas, at recurrence the tumor is abundantly infiltrated by peripheral MDMs, which are unlikely to be detected by ¹⁹F MRI based on the lack of peripheral cell labelling by PFCE-NP at this late stage (fig. S2F). As such, we reasoned that an initial PFCE-NP⁺ TAM population (likely MG predominantly) remains in the residual tumor bed following RT treatment and forms a discrete TAM cluster, while the recurrent outgrowing glioma is infiltrated by new (PFCE-NP-unlabeled) myeloid cells originating from the periphery.

Therefore, in order to capture the integrated cellular, temporal and spatial complexity of TAM dynamics until recurrence, we decided to investigate the potential use of multispectral ¹⁹F MRI, allowing the detection of temporally-distinct cell populations (44, 45). Glioma-bearing mice were injected with a single administration of PFCE-NP before RT (single dose of 10 Gy), and monitored by conventional ¹H MRI until glioma recurrence. At recurrence, these mice were injected with a second, distinct perfluorocarbon-containing nanoparticle (perfluoro-tert-butylcyclohexane (PFTBH)-NP), which emits a fluorine resonance peak at a separate frequency from PFCE, and a final ¹H and ¹⁹F MRI was performed (Fig. 6D and fig. S6B) (23). Interestingly, we found that the ¹⁹F signal from PFTBH-NP mainly covered a region of the tumor that did not show signal from the original PFCE-NP (Fig. 6, E and F). Moreover, the cumulative ¹⁹F signal volume was significantly higher than the original PFCE-NP ¹⁹F signal volume alone (Fig. 6G), showing a volumetric dynamic that was similar to conventional ¹H MRI monitoring, where larger tumor volumes were detected at recurrence (Fig. 5B). Of note, while the ¹⁹F SNR of the PFCE and PFTBH compounds was similar in the liver, it was higher for PFCE in the tumor, possibly as a consequence of the initial PFCE concentration increase after RT (Fig. S6C and fig. S6D). Accordingly, we inferred that TAMs not only shift their relative proportion between MG and MDMs following RT, but that this powerful multispectral ¹⁹F MRI strategy could reveal alterations in their spatial organization which potentially differ in untreated and recurrent gliomas, which we therefore investigated further.

The distribution pattern of TAMs within tumors changes following RT treatment.

We explored how the spatial and temporal distribution of TAMs changes following RT treatment by analysis of tissue sections. IF staining of PDG-Ink4a/Arf KO gliomas in the CX3CR1 lineage-tracing background showed differences in the spatial distribution of TAMs between untreated and recurrent tumors, where substantial MDM-rich areas could be observed specifically at recurrence (Fig. 7A). In order to quantify this observation, we analyzed the average distance between MDMs and MG (Fig. 7B), and found that MDMs were significantly more distant from MG in recurrent tumors compared to untreated gliomas, indicative of this clustering phenomenon. To assess a potential spatial mutual exclusion between the two cell types, we analyzed the frequency of MG in a region of interest defined around MDMs (termed MDM-ROI) in untreated and recurrent tumors (Fig. 7C). Interestingly, we found a significantly lower abundance of MG in MDM-rich areas at recurrence (Fig. 7D). Collectively, these results showed that while MDMs and MG are generally evenly distributed within untreated tumors, at recurrence we observe the spatial emergence of localized clusters of distinct TAM populations, as initially indicated by the ¹⁹F MRI analyses.

While these analyses revealed different spatial patterns of TAMs in untreated versus RT-recurrent tumors, it did not enable the temporal discrimination of the sequence of cell infiltration throughout the experimental time course. Given that RT has been reported to lead to hemolysis and hemoglobin release in other contexts (46, 47), we assessed if this process is also evident in gliomas following RT, and whether iron uptake by specific cells could thereby mark them in a temporal manner. We therefore stained PDG-Ink4a/Arf KO glioma sections with Prussian Blue (PB) to visualize iron deposition. While there were only rare PB⁺ cells in untreated tumors, we found a peak of PB⁺ cells at 7 days after RT (Fig. 7E). To identify the cellular source of the PB signal, we multiplexed PB and IF staining (fig. S7A) and found MDMs to be the main cell type accumulating iron, while no PB⁺ MG were observed (fig. S7B). To confirm these findings, we analyzed a published gene expression dataset of MG and MDMs in untreated, 5 day-irradiated and RT-recurrent gliomas (5). GSEA indeed showed increased iron uptake-related processes at 5 days post-RT and at recurrence specifically in MDMs, but not in MG, thus supporting our observation of an increased frequency of PB⁺ cells following RT treatment (fig. S7C). Together, these results revealed the emergence of a temporally-defined PB⁺ population (mainly MDMs) only after RT.

Finally, we investigated if the PB⁺ cells remained in proximity to one another in recurrent gliomas. We analyzed their frequency in the whole tumor area, as well as in a defined ROI around PB⁺ cells (termed PB⁺ ROI) (fig. S7D). We found that the frequency of PB⁺ cells in the PB⁺ ROI was higher in recurrent than untreated tumors (Fig. 7F). This indicates that these cells cluster together during tumor outgrowth and form a spatially defined niche, despite their generally low abundance overall (Fig. 7E). In sum, through these analyses, we found that in recurrent tumors there is a higher infiltration of MDMs which localize distally from MG. PB⁺ cells (mainly MDMs) are enriched after RT treatment and also cluster together in the larger recurrent tumors. These results show that different TAM populations, in addition to shifting their relative abundance in a dynamic manner, can also vary in spatial distribution in a time-dependent manner, as revealed by our multispectral ¹⁹F MRI strategy (Fig. 7G).

DISCUSSION

MRI is indispensable in neuro-oncology practice, yet quantitative, standardized and robust MRI-based biomarkers are currently sparse (16). Recent clinical studies demonstrated the potential of MRI in predicting the response to antiangiogenic treatment in pediatric and adult brain tumors (48, 49). Quantitative characterization of vascular properties is a common MRI application in the imaging of brain tumors, due to the ability of gadolinium-based contrast agents to penetrate and enhance those tumor regions with a disrupted BBB (50, 51). Nonetheless, the vasculature is just one component of the complex brain TME (1). Despite the high abundance of TAMs in gliomas (3, 4), and their importance in establishing an immunosuppressive TME (52), with potential direct consequences on the effectiveness of novel immunotherapeutic strategies in patients (53), TAM abundance and distribution can currently only be assessed following an invasive surgical procedure to remove the tumor.

In this study, we harnessed the power of ^{19}F multispectral MRI in preclinical glioma and brain metastasis models to show the technological feasibility of longitudinally and non-invasively imaging small inflamed brain tumors *in vivo* with a clinical scanner at high spatial resolution. These results highlight the translational potential of this strategy to expand the MRI repertoire used to classify diverse brain malignancies (54). Interestingly, we found substantial differences in the ^{19}F signal distribution between the preclinical glioma and brain metastasis models, underlining a potential relevance for distinguishing these two brain tumor types. Indeed, this result is supported by the lower overall TAM abundance observed in both preclinical BrM models and patient BrM tissues compared to gliomas (3, 4, 55), which can thus explain the observed lower accumulation of PFCE-NP in the BrM model. Moreover, the presence of the BBB plays a crucial role in regulating the delivery of the PFCE-NP, which was more efficient in the primary breast tumor setting compared to the breast-BrM model.

To date, the application of PFCs to image immune cells in cancer has largely relied on the *ex vivo* labelling of specific cell types in the context of monitoring cell-based therapies, such as adoptive T-cell transfer and DC-based cancer vaccination (56, 57). *In vivo*, only a handful of studies have explored the distribution of injected PFC-NP to image myeloid cells (25, 34, 37, 58-60), and the sub-cellular composition of the labelled myeloid cells has been minimally investigated (61). Moreover, the extent of brain microenvironmental heterogeneity has been underscored by recent single cell analyses, with potential translational implications (62). In this study, we found that

PFCE-NP in preclinical glioma models label several myeloid cell subpopulations, mostly comprising resident MG and peripheral MDMs, which also displayed a significant heterogeneity and likely contain additional cell subpopulations. Importantly, both MG and MDMs were labelled directly within the tumor and were not evidently replenished by newly infiltrating immune cells in the weeks following PFCE-NP administration. Moreover, our gene expression analysis revealed rhodamine-PFCE-NP⁺ TAMs to be characterized by specific metabolic signatures, which may relate to critical phenotypes and functions (42, 63, 64), and was associated with their enrichment in the perivascular niche. We also assessed several gene signatures specific to classically- or alternatively-activated macrophages (65-69), also termed M1- or M2-like macrophages, which did not reveal a specific enrichment of any of these signatures in the PFCE-NP⁺ cells (data not shown). These findings emphasize the importance of a detailed characterization of the TAM subsets that uptake PFCE-NP, and highlight potential future questions exploring the role of additional macrophage populations, including CNS border-associated macrophages, and the employment of single-cell analysis (70).

Our data also showed that TAMs are the predominant, though not the sole cell population taking up PFCE-NP. Non-immune cells were the second largest PFCE-NP⁺ population, including endothelial cells, thereby indicating an active role of the vasculature in the trafficking of these NP *in vivo*. Uptake in other non-immune cells included a small proportion of cancer cells and potentially other non-immune non-malignant cell types. Indeed, rapidly dividing cells have been shown to actively engulf nanoparticles by macropinocytosis (71, 72). Moreover, brain-resident astrocytes also have phagocytic ability (73). Thus, future studies will be important to further explore the precise ontogeny of the rare non-immune cell types incorporating NP, as well as the underlying cellular mechanism for NP uptake. While multiple studies have demonstrated a clear role for phagocytosis and macropinocytosis in PFC-NP uptake *in vitro* (26, 27), further research is required to better understand this process *in vivo*. Of note, we did not find any increased expression of genes involved in phagocytosis in the rhodamine-PFCE-NP⁺ TAMs (data not shown) (74). As such, the IVM method presented in this study might be a valuable approach to address these open questions and aid in designing cell type-specific NP to selectively label and target only the population of interest.

TAM content and composition is in constant flux and adaptation during tumor growth and in response to therapies (5, 8). In this context, ¹⁹F MRI represents a powerful strategy to temporally

and spatially track distinct inflammatory dynamics in RT-recurrent tumors by performing multispectral imaging using PFCE-NP and PFTBH-NP. This allowed us to gain new insights into the presence of different TME niches not only before treatment and at recurrence, but also during tumor dormancy, when the tumor had regressed and tumor volume was stable. Emergence of therapy resistance from a dormant state is known to be a key step involving TAM-mediated mechanisms in response to different therapeutic interventions (5, 11), although a non-invasive clinical assessment of TAMs in dormant tumors has not been achievable to date. Our analyses revealed that gliomas not only shift the ratio of MDM:MG in response to RT, but also differ in the spatial distribution of these distinct cell populations. This finding has relevance for deeply understanding the complexity of the brain TME, by integrating critical temporal and spatial parameters. In this context, it will be important to assess if these TAM-defined microenvironmental niches respond differently to specific treatments, for example. Moreover, we also identified an RT-triggered iron-rich TAM population that occupies a specific niche from 7 days after radiation therapy through to tumor recurrence. Iron is an essential metal micronutrient and its metabolism in tumors is regulated by TAMs, with a direct impact on tumor growth and on the immune response of macrophages themselves (75), suggesting that this specific cell population may play an important role in adaptive resistance.

Nanoparticle-based drug delivery and anti-angiogenic treatments have been widely studied in brain tumors with several objectives and potential applications. The first is to improve the delivery of compounds with a poor pharmacokinetic profile, leading to optimal drug release and potentially reducing drug side-effects (76). The second is to normalize the vasculature, thereby resulting in improved drug delivery (39). The unique structure of the BBB, however, requires a careful and meticulous investigation of the effect of vascular integrity on drug delivery (39). Vessel normalization has been shown to enhance the efficacy of chemotherapeutic agents in preclinical glioma models (77). However, a study of multiple pediatric brain tumor models, driven by distinct oncogenic alterations, revealed a differential impairment of the BBB, which resulted in effective chemotherapy delivery only in medulloblastoma with disrupted vessels (78). Our findings in this study directly connect the heterogeneity of the vasculature with the extent of PFCE-NP accumulation. The NP only accumulated in areas of dysmorphic vessels, highlighting the notion that vessel normalization in brain tumors needs to take into consideration the type and size of any additional combinatorial drug treatments. ¹⁹F MRI can thus represent a potential MRI-based method to gain important information regarding the extent and heterogeneity of BBB leakage,

which is conventionally assessed using gadolinium-based contrast agents at present, and could be linked to the abundance, phenotype and cellular identity of TAMs.

In conclusion, we propose multispectral ^{19}F MRI as a powerful strategy to non-invasively and longitudinally explore brain TME composition and functionality. In the future, it will be of great interest to assess its diagnostic and prognostic impact for brain malignancy-related processes, including pseudo-progression, pseudo-regression, and necrotic inflammation to inform the clinical management of the disease, as well as its ability to predict therapy response to targeted treatments, including in other CNS diseases.

MATERIALS AND METHODS

Study design

The aim of this study was to longitudinally and non-invasively monitor TAM dynamics with multispectral ^{19}F MRI over the course of tumor response to radiotherapy. The sample size for longitudinal imaging trials ($n=8$ to 15 mice) was based on previous experience using these glioma models (5, 10, 11, 29) and planned using the statistical program OpenEpi (79). ^{19}F signal monitoring was the primary outcome of these experiments. These data were supported by tissue staining, flow cytometry, *ex vivo* and *in vivo* imaging and RNA sequencing to further understand the kinetics and distribution of the nanoparticles and the underlying biological mechanisms of the MRI-based observations. The choice of defined individual time points for these analyses was based on previously published data on nanoparticle kinetics (22, 40) and sample size ($n=3$ to 8) was defined as described above. Age-matched mice were assigned to experimental cohorts based on matching tumor volumes, and data presented include all outliers. Investigators were not blinded when treating and monitoring the animals. Blinding was applied during all data analysis. Biological replicates are indicated in the figure legends by n , together with the statistical analysis applied. Two or more independent trials or experiments were performed for all preclinical models, with the exception of the primary breast cancer model, which was performed in a single experimental cohort. All animal studies were reviewed and approved by the Institutional Animal Care and Use Committees of the University of Lausanne and Canton Vaud, Switzerland.

Animals, cells and tumor models

Animals

The Nestin-Tv-a;*Ink4a/Arf*^{-/-} mouse line has been previously described (80) and was generously provided by Dr. Eric Holland, USA. *Cx3cr1:CreER-IRES-YFP* mice (C57BL/6J background; Jackson Labs) were crossed with Rosa26:lsI-TdTomato reporter mice (C57BL/6J background; Jackson Labs), and with Nestin-Tv-a;*Ink4a/Arf*^{-/-} mice (29). For the *Cx3cr1:CreER-IRES-YFP* Rosa26:lsI-TdTomato lineage tracing system, 3 to 4 week-old mice were injected twice, 48 hours apart, intraperitoneally with 1 mg of tamoxifen citrate (Sigma-Aldrich) dissolved in sunflower seed oil (Sigma). Mice were used for intracranial injection surgery 3 weeks after tamoxifen administration (see “Glioma model” section below). Wild-type female C57BL/6J mice were used for the PyMT-BrM3 brain metastasis (BrM) and primary breast tumor models. All mice were bred

within the University of Lausanne animal facilities, and all animal studies were first approved by the Institutional Animal Care and Use Committees of the University of Lausanne and Canton Vaud, Switzerland.

Cells

For glioma induction, DF1 chicken fibroblasts were obtained from the ATCC. RCAS vectors expressing PDGFB-HA or PDGFB-HA-SV40-GFP were kindly provided by Dr. Tatsuya Ozawa and Dr. Eric Holland, USA (28, 81). DF1 cells were transfected with the RCAS vectors using FuGENE 6 (Promega) according to the manufacturer's instructions. PDGFB-HA-SV40-GFP DF1 cells were sorted by flow cytometry to collect GFP⁺ cells and to subsequently culture a stable GFP-positive DF1 cell line. All cell lines were cultured in DMEM (Life Technologies) supplemented with 10% fetal bovine serum (Life Technologies) under standard conditions. For brain metastasis induction, the murine parental 99LN cell line was derived from a metastatic lymph node lesion that arose in the MMTV-PyMT (murine mammary tumor virus; Polyoma middle T antigen) breast cancer model (C57BL/6J background) (82). This cell line was sequentially selected *in vivo* for brain-homing capacity (29), for a total of three times, resulting in the new PyMT-BrM3 variant used herein. The PyMT-BrM3 cell line was maintained in DMEM/F-12 medium containing 10% fetal bovine serum with 1% l-glutamine and 1% penicillin/ streptomycin.

Glioma model

4.5 to 7 week-old mice were intracranially injected as previously described (10, 11, 28, 29). Briefly, mice were fully anesthetized using isoflurane inhalation anesthesia (2% isoflurane/O₂ mixture), and a mixture of 2% lidocaine (Streuli Pharma) and 0.5% bupivacaine (Carbostesin; Aspen Pharma Schweiz) was applied as a local analgesic (50 µl per mouse), and 0.3 mg/ml buprenorphine (Temgesic; Indivior Schweiz) was given subcutaneously as a systemic analgesic (100 µl per mouse). Using a stereotactic apparatus, cells were injected into the right frontal cortex (2 mm frontal, 1.5 mm lateral from bregma, 2 mm deep). Mice were injected with 2 x 10⁵ RCAS-PDGFB-HA or PDGFB-HA-SV40-GFP DF1 cells. The skin incision was sealed with Vetbond tissue adhesive (3M), and the mouse was placed on a heating pad and monitored until fully recovered from anesthesia. Finally, Bepanthen cream (Bayer) was applied on the incision site before placing the animal back in the cage, and each mouse was followed by regular monitoring.

Generation of experimental brain metastasis

The initiation of brain metastasis from the PyMT-BrM3 line was performed as previously described for other BrM derivatives (29, 83, 84). Briefly, PyMT-BrM3 cells were resuspended in HBSS (Life Technologies) and 1×10^5 cells were inoculated into the left cardiac ventricle of 6-10 week-old female C57BL/6J mice.

Generation of experimental primary breast tumor model

For the generation of primary breast tumors, 6-10 week-old female C57BL/6J mice were anesthetized using isoflurane inhalation and 7×10^5 PyMT-BrM3 cells resuspended in 50% Matrigel (Corning Cat. no 356231) were injected orthotopically in the mammary fat pad. Mice were regularly monitored, and tumor volumes assessed twice per week using calipers. Tumor volumes were calculated as $\text{vol} = (\text{width}^2 \times \text{length})$.

Cranial window surgery

Cranial window surgery was performed as previously described (41). Mice were fully anesthetized using isoflurane inhalation anesthesia (2% isoflurane/O₂ mixture) and prepared for surgery by shaving and cleaning the head with 70% ethanol pads (Fisher Healthcare) and 10% betadine pads (Purdue Products L.P.). A mixture of 2% lidocaine (Streuli Pharma) and 0.5% bupivacaine (Carbostesin; Aspen Pharma Schweiz) was applied as a local analgesic (50 μ l per mouse), and 0.3 mg/ml buprenorphine (Temgesic; Indivior Schweiz) was given subcutaneously as a systemic analgesic (100 μ l per mouse). A longitudinal incision of the skin was made between the occiput and forehead, and the skin covering the skull was cut in a circular manner, by removing approximately 3 mm of the skin edges on each side. After cleaning and drying the skull with a cotton swab, the bone was etched mechanically with a scalpel (by making a pattern of crosses) and chemically by applying 35% phosphoric acid solution (Santa Cruz Biotechnology) with a cotton swab. The skull was then cleaned several times with Ringer's solution (Dutscher), and the mouse was placed into a stereotactic device with a three-axis micromanipulator and an integrated heating pad (Stoelting). A 3-mm craniotomy was made using a 3-mm biopsy punch (Integra Miltex), ensuring precise fitting of the imaging window. The exposed cortical surface was kept moist using Ringer's solution. DF1 cells were injected into the brain parenchyma at the craniotomy site as described in the previous section. The brain surface was sealed with a 0.085-mm-thick 3-

mm diameter coverslip (Multichannel Systems) that was glued to a 0.085-mm-thick 5-mm diameter coverslip (Multichannel Systems) using Norland optical adhesive 61 (AMP Technica). The outer edges of the 5-mm coverslip were used to fix the imaging window to the skull using super glue (Loctite). A small head bar was fixed using super glue (Loctite), allowing fixation of the mouse's head during the subsequent intravital imaging experiments. Lastly, dental acrylic glue (Kulzer) was applied on the skull surface, covering also a small rim of the 5-mm coverslip. The animal was then placed on a heating pad and monitored until it had fully recovered and was returned to the cage, followed by regular monitoring.

Treatments

Perfluorocarbons

An initial PFC emulsion based on 10% weight/volume (wt/vol) perfluoro-15-crown-5 ether (PFCE) was prepared in-house as described previously (20% wt/vol emulsions were used for experiments with the primary breast tumor model) (22, 40). The emulsion contains nanoparticles with a mean size of 200 nm, and produces a single spectral line at -92.8 ppm. A second, similar PFCE emulsion was prepared with rhodamine to enable fluorescence-activated cell sorting. A third PFC emulsion based on 60% wt/vol perfluoro-t-butylcyclohexane (PFTBH) (23) was provided by Aurum Biosciences (Glasgow, United Kingdom). PFTBH produces a singlet spectral line at -61.5 ppm (a 3650 Hz shift from PFCE) that is used for imaging, as well as a multiplet that ranges from -115 to -144 ppm (23).

Intravenous injections

A red heat lamp (Beuer) was placed at 15 to 20 centimeters distance from the cages housing the mice to be injected. After 15 minutes, a mouse was removed from the cage and placed into a restrainer (Indulab) and held in a firm position through the nose holder, allowing proper breathing and minimal movement of the animal. The tail was gently cleaned with 70% ethanol pads (Fisher HealthCare) to disinfect the skin and better visualize the tail vein. The mouse was injected with a 29-gauge (G) needle syringe (BD Medical) in the right or left lower tail vein. For PFCE-NP and rhodamine-PFCE-NP, 10 μ L/g were injected. For PFTBH-NP 3.3 μ L/g were injected. The difference in the amount of injected NP accounts for 1) the difference in wt/vol %, and 2) the

different amount of fluorine atoms contributing to the ^{19}F signal. For lectin DyLight649 (Vector), 100 μL was injected via the tail vein for each mouse.

BLZ945 treatment

For *in vivo* experiments, BLZ945 (purchased from Selleck) was dissolved in 20% Captisol (w/v) (Ligand Pharmaceuticals) in H_2O and stirred overnight to obtain a clear solution. The pH of the solution was lowered to 2.2 with hydrochloric acid (Honeywell Fluka) to allow proper dissolution. Dissolved BLZ945 was administered daily at 200 mg/kg by oral gavage, as previously described (35).

Radiotherapy

Tumor-bearing mice were fully anesthetized using isoflurane inhalation anesthesia (2% isoflurane/ O_2 mixture). Radiotherapy of the head was performed with a X-RAD SmART instrument (Precision X-Ray) equipped with 1x1 cm collimator to limit radiotherapy to the tumor area only. First, a live-imaging CT scan of the head was performed to place the collimator in the correct position to irradiate the brain (cerebellum and the upper respiratory tract were left outside the field of view). A beam of 5 Gy was dosed laterally for the animal, from the right side and the left side respectively, for a total of 10 Gy.

Tissue analysis

Brain slice harvesting and 2-photon microscopy imaging

Mice were sacrificed by terminal anesthesia using pentobarbital (CHUV, Lausanne, Switzerland), followed by transcardial perfusion with PBS. Tumor-bearing brains were harvested and placed on ice in “slicing medium” (minimum essential media 2 mM L-glutamine (MEM GlutaMAX, Life Technologies), 4.5 mg/mL glucose (Life Technologies), 100 U/mL penicillin-streptomycin (P/S, Life Technologies)). When possible, the tissue was kept in the dark to preserve the fluorophores. The brain was then fixed on the specimen plate of a vibratome (Leica) with super glue (Loctite). The brain was held in place with 2% agar cubes to additionally support the tissue while slicing, and submerged into “slicing medium” in the buffer tray. The vibratome was set at a moving speed of 0.5 mm/s, a vibration amplitude of 1 μm , and 425- μm -thick coronal slices were cut sequentially

and placed into “culturing medium” (MEM GlutaMAX, 4.5 mg/mL glucose, 100 U/mL P/S, 25% HBSS (Life Technologies), 25% heat-inactivated normal horse serum; re-supplement: 1X GlutaMAX (Life Technologies), 1X non-essential amino acids (Life Technologies), 1:50 1M HEPES (Life Technologies)) on ice. Three to four slices per mouse were placed on a microscope slide (Fisher Scientific) and enclosed by a layer of Dowsil 732 multi-purpose sealant (Dow) to create a small bucket which was then filled with a small amount of culturing medium, and finally enclosed by a coverslip (Menzel-Gläser). Images were acquired using an upright Leica TCS SP8 DIVE multi-photon microscope (Mannheim, Germany) equipped with a 16x (HC FLUOTAR L N.A. 0.6 FWD 2.5 mm) multi-immersion objective. GFP and rhodamine were excited with a wavelength of 960 nm, and detected between 500-540 nm and 580-650 nm respectively. Lectin DyLight649 was excited with a wavelength of 810 nm and detected at 690-800 nm (a second detector was set as an “empty channel” on 300-475 nm to detect any broad autofluorescence signals).

Immunofluorescence staining and imaging of tissue sections

10 µm tissue sections were thawed for 10 minutes (18 µm thickness for rhodamine-PFCE-NP samples), and circles were drawn around the tissue with a PAP pen (Daido Sangyo). After 5 minutes washing in 1X PBS (Bichsel), the slides were permeabilized with 0.1% Triton X-100 (AppliChem) diluted in 1X PBS for 10 minutes at room temperature (RT) (rhodamine-PFCE-NP samples were not permeabilized to avoid any signal loss). Slides were then washed 3x5 minutes with 1X PBS, and then incubated with filtered blocking buffer for 1 hour at RT (1.5 hours for 18 µm sections). The blocking buffer consisted of 1X PBS, 0.2% bovine serum albumin (Jackson ImmunoResearch), 10% donkey normal serum (EMD Millipore), 10% goat normal serum (Merck); when using goat primary antibodies, BSA and goat serum were omitted from the blocking buffer mix. Sections were then incubated with 250 µL/ section primary antibody mix (Table 1) in dilution buffer (1:1 mix of 1X PBS and blocking buffer) at 4°C overnight. The next day, slides were washed 3x10 minutes with 1X PBS and then incubated with the secondary antibody mix (Table 1) in dilution buffer including 1:5000 DAPI (Life Technologies) for 1 hour at RT (1.5 hours for 18 µm sections). For membrane staining, sections were additionally incubated for 30 minutes at RT with 1:200 1mg/mL Alexa Fluor 488 wheat germ agglutinin (WGA, Thermo Fisher). Slides were finally washed 3x10 minutes in 1X PBS and mounted with Dako mounting medium (Agilent) and a coverslip (Menzel-Gläser). Of note, rhodamine-PFCE-NP labeled tissue sections were carefully selected from brain slices that displayed a robust rhodamine signal by 2-photon microscopy

imaging (see previous section). Stained tissue sections were imaged with an Axio Scan.Z1 slide scanner (Zeiss) equipped with a Colibri 7 LED light source (Zeiss) using a Plan-Apochromat 20x/0.8 DIC M27 coverslip-corrected objective (Zeiss). All slides from the same staining panel were digitalized using the same acquisition settings. All washes were performed in a slide bucket, while all incubation steps were performed in a humidified chamber. One tissue section was stained with primary antibodies, while the adjacent section on the same slide was stained with secondary antibodies alone to assess non-specific antibody binding and any background signal.

Flow cytometry

Mice were sacrificed by terminal anesthesia using pentobarbital (CHUV, Lausanne, Switzerland), followed by transcardial perfusion with PBS. When possible, the tissue was kept in the dark to preserve the fluorophores. The brain tumor was macro-dissected and dissociated using the Brain Tumor Dissociation Kit (Miltenyi). The dissociated tissue was filtered through a 40 µm mesh filter and then underwent myelin removal using the Myelin Removal Beads Kit (Miltenyi). The resulting myelin-free single cell suspension underwent red blood cell lysis for 10 minutes on ice using 10x red blood cell lysis buffer (Biolegend). The single cell suspension was stained with the Zombie-near-infrared fixable viability kit (Biolegend) for 20 minutes at room temperature (RT), washed with FACS buffer (2 mM EDTA (Life Technologies) and 0.5% BSA (Jackson ImmunoResearch) in PBS (Bichsel) and then FC-blocked (BD Biosciences) for 30 minutes on ice. After washing with FACS buffer, cells were incubated with directly-conjugated antibodies (Table 1). Stained samples were washed three times with FACS buffer and acquired on a BD Fortessa at the Flow Cytometry Core Facility of the University of Lausanne. FlowJo v10.7.1 (BD) was used for analysis, including the tSNE plugin for clustering analysis. The following gating strategy was applied: alive cells (Zombie⁻) were categorized into myeloid cells (CD11b⁺CD45⁺), lymphoid cells (CD11b⁻CD45⁺) and non-immune cells (CD11b⁻CD45⁻). Myeloid cells were categorized into monocytes (Ly6G⁻Ly6C⁺), neutrophils (Ly6G⁺Ly6C⁺) and TAMs (Ly6G⁻Ly6C⁻), which were further classified as MG (CD49d⁻) and MDMs (CD49d⁺). Lymphoid cells were categorized into T cells (CD3⁺), B cells (CD19⁺) and NK cells (NK1.1⁺). Non-immune cells were categorized into CD31⁻ cells and CD31⁺ endothelial cells.

Prussian Blue staining and imaging

Prussian blue (PB) staining was performed on freshly-thawed 10 μm sections, or after IF staining for multiplexing analysis. Sections were washed 2x10 minutes with deionized H_2O and then incubated 15 minutes with a 1:1 solution of freshly mixed hydrochloric acid solution (Abcam) and potassium ferrocyanide solution (Abcam). After 2x5 minutes washes with deionized H_2O , sections were stained 3 minutes with nuclear fast red solution (Abcam). Sections were finally washed 4x5 minutes with deionized H_2O and dehydrated with 95% and 100% ethanol solutions (Reactolab) and xylene (Reactolab), before mounting with Pertex mounting medium (Histolab) and a coverslip (Menzel-Gläser). Slides were left to dry for 24h before imaging with an Axio Scan.Z1 slide scanner (Zeiss) equipped with a Colibri 7 LED light source (Zeiss) using a Plan-Apochromat 20x/0.8 DIC M27 coverslip-corrected objective (Zeiss).

Ex vivo rhodamine-PFCE-NP treatment

Mice were sacrificed by terminal anesthesia using pentobarbital (CHUV, Lausanne, Switzerland), followed by transcardial perfusion with PBS. The brain tumor was macro-dissected and a piece of contralateral brain was taken from the posterior part of the brain hemisphere opposite to the tumor. Both tissues were dissociated using the Brain Tumor Dissociation Kit (Miltenyi). The dissociated tissue was filtered through a 40 μm mesh filter and then underwent myelin removal using the Myelin Removal Beads Kit (Miltenyi). The resulting myelin-free single cell suspension underwent red blood cell lysis for 10 minutes on ice using 10x red blood cell lysis buffer (Biolegend). The resulting cell suspension was plated at a concentration of 1000 cell/ μL in DMEM (Life Technologies) supplemented with 10% fetal bovine serum (Life Technologies) and cultured under standard conditions. Rhodamine-PFCE-NP were supplemented in the medium at 1:10,000 dilution.

In vivo mouse imaging

^1H and ^{19}F MR imaging acquisition

All MRI experiments were performed on a 3T clinical system (MAGNETOM Prisma, Siemens Healthineers, Erlangen, Germany). A 35 mm-diameter transmit/receive birdcage radiofrequency (RF) coil, tunable to both the ^{19}F and ^1H frequencies (Rapid Biomedical, Rimpar, Germany), was

used for both excitation and signal detection. Two days after the PFC-NP injection, the animals were anesthetized with 2.5% isoflurane in oxygen for 1–2 minutes. Anesthesia was maintained with 1.5–2% of isoflurane for the duration of the scan. The body temperature was monitored with a rectal probe and maintained at 37.0 ± 0.5 °C with a tubing system circulating warm water, while the respiratory activity was monitored by means of a respiration pillow placed below the mouse abdomen (all SA Instruments, Stony Brook, New York, USA). An external reference tube with a known concentration of PFCE-NP (18.95 mM) in 2% wt/vol agar gel (Life Technologies) was created and used for absolute quantification. The tube was carefully placed diagonally below and to the side of the brain of the animal (i.e. below the level of the shoulders) such that any artifactual signal emitted from this reference did not interfere with the signal from the brain. In the dual-PFC experiments, a second probe with PFTBH-NP (40 mM) was placed adjacent to the other shoulder of the animal. Multi-planar low-resolution scout scans were then performed for anatomic localization. For glioma and primary breast tumor model imaging, a high-resolution T_2 -weighted 3D turbo spin echo (TSE) scan was acquired in an axial orientation. The following pulse sequence parameters were used: repetition time TR = 4500 ms, echo time TE = 80 ms, echo train length (ETL) = 32, pixel bandwidth BW = 130 Hz/pixel, field of view (FOV) = $60 \times 60 \times 32$ mm³, voxel size = $0.16 \times 0.16 \times 1$ mm³, number of slices = 32, slice oversampling = 12.5%, acquisition time T_{acq} = 32min19s. For metastasis imaging, mice were injected intraperitoneally (i.p.) with 150 μ l Gadobutrol (Gadovist, 1 mmol/mL, Bayer) 10 min before the measurement. A high-resolution T_1 -weighted 3D gradient-recalled echo (GRE) scan was acquired with the following parameters: TR = 280 ms, TE = 3.4 ms, BW = 320 Hz/pixel, FOV = $60 \times 60 \times 20$ mm³, voxel size = $0.21 \times 0.21 \times 1$ mm³, number of slices = 20, slice oversampling = 10%, T_{acq} = 29min33s. ¹⁹F MR images of PFCE were obtained with a 3D TSE pulse sequence with the following sequence parameters optimized for maximal SNR in 30 minutes (85): TR = 2460 ms, TE = 13 ms, BW = 130 Hz/pixel, ETL = 43, FOV = $100 \times 100 \times 16$ mm³, voxel size = $0.78 \times 0.78 \times 1$ mm³, number of slices = 16, slice oversampling = 12.5%, number of signal averages NA = 14, T_{acq} = 30min57s. The center of the 3D volume was placed at the same position as the ¹H 3D volume. When PFTBH was imaged, the ¹⁹F resonance frequency was shifted to the appropriate frequency and the same 3D TSE pulse sequence was used, but with TR = 2850 ms, NA = 9, ETL = 35, and T_{acq} = 30min44s.

PFCE phantom preparation

Different PFCE concentrations were prepared in 2% wt/vol agar gel (Life Technologies) in 0.5 mL Eppendorf tubes. To demonstrate reliable quantification of the ^{19}F signal, phantom measurements were performed using the same PFCs as for the *in vivo* experiments. MRI data were acquired with the same parameters described above.

MRI monitoring of tumor volume

Monitoring of tumor growth for non-quantitative MR imaging was performed using a 3 Tesla small animal MR scanner (Bruker BioSpin MRI, Ettlingen, Germany) with an 82-mm volume coil as transmitter, combined with a 2 x 2 mouse brain phased array surface coil for signal reception. The mouse was fully anaesthetized with 1-2% isoflurane/oxygen inhalation and placed on the imaging bed with the head held in place below the surface coil, while monitoring respiratory rate and temperature. Data acquisition was performed using the Paravision 360 v2.0 software (Bruker BioSpin MRI, Ettlingen, Germany). A 3-slice localizer was performed to assess the mouse head position. For glioma-bearing mice, 2D turbo rapid acquisition relaxation enhancement (Turbo-RARE) T_2 -weighted acquisition was performed with the following pulse sequence parameters: TR = 3000 ms, TE = 75 ms, NA = 6, number of slices 10, slice thickness (ST) = 0.7 mm, FOV = 20 x 20 mm², pixel size 0.156 x 0.156 mm², (ETL= 12, T_{acq} = 3min) with images being acquired in axial planes. After imaging, the mouse was returned to the cage and closely monitored until it regained consciousness. Volumetric analysis of the gliomas was performed on MRI DICOM files using the MIPAV software (National Institutes of Health, USA). For BrM-bearing mice, animals were injected intraperitoneally (i.p.) with 150 μl Gadobutrol (Gadovist, 1 mmol/mL, Bayer) 10 min before the measurement. Fast low angle shot magnetic resonance imaging (T_1 -FLASH) T_1 -weighted images were acquired with the following pulse sequence parameters: TR = 253.3 ms, TE = 6.3 ms, NA = 6, number of slices = 10, ST = 0.7 mm, FOV = 20 x 20 mm², pixel size 0.156 x 0.156 mm², T_{acq} = 3min14sec.

Intravital imaging

Mice were sedated using isoflurane inhalation anesthesia (3% isoflurane/O₂ mixture). Mice were fixed with a head-bar to a custom-designed mouse holder, and the concentration of isoflurane

was lowered to 0.8-1.2% to keep the mice lightly sedated, characterized by a constant and non-forced breathing pattern. The mouse was placed in the climate chamber surrounding the microscope, keeping the entire stage of the microscope and the objectives at 34°C. Imaging was performed on an upright Leica TCS SP8 DIVE multi-photon microscope (Mannheim, Germany) with an InSight X3 tunable laser (Spectra Physics) and two non-descanned hybrid 4Tune detectors. GFP and rhodamine were excited with a wavelength of 960 nm, and detected between 500-540 nm and 580-665 nm respectively. All images were acquired with a 16× (HC FLUOTAR L N.A. 0.6 FWD 2.5 mm) multi-immersion objective. The objective lens was corrected for imaging with Immersol W 2010 (Carl Zeiss) and a coverslip thickness of 0.17 mm. For each mouse, a tile scan of the whole cranial imaging window (CIW) was taken before, immediately after, 6h and 24h after PFCE-NP injection.

Data analysis

MR Image Analysis

¹H images produced by the MR scanner in dicom format were copied, while the ¹⁹F images were reconstructed from raw data in Matlab (Mathworks, Natick, Massachusetts, USA) to ensure that the background noise was correctly digitized. All subsequent image analyses were then performed in Matlab. The ¹H and ¹⁹F MR images were post-processed in several semi-automated steps to obtain reproducible and consistent PFC quantifications. The tumor outline was manually delineated in the high-resolution ¹H images to calculate the ¹H tumor volume. The slice numbers that visually contained tumor tissue were retained to constrain the ¹⁹F calculations. In the stack of ¹⁹F images, a rectangular region of interest (ROI) was drawn at the edge of the image (where no tissue was present) to determine the background noise level for subsequent thresholding. The ¹⁹F images were then flattened into a maximum intensity projection (MIP) on which broad ROIs were drawn around the tumor, reference tube, and liver. These MIP ROIs were then copied to all slices. Simultaneously, the ¹⁹F images were automatically thresholded at 6X the standard deviation of the previously determined background noise level in order to generate a mask that satisfies the Rose criterion (86), avoids the inclusion of low-amplitude ghosting artifacts, and thus only contains voxels with a high ¹⁹F signal. To reproducibly generate a ROI that only included the voxels with signal from the tumor, the retained ¹H slices, the manually drawn ¹⁹F MIP ROI, and the ¹⁹F threshold mask were multiplied. This procedure was then repeated to generate selective

liver and reference tube ROIs. The average ^{19}F signal in these ROIs was divided by the ^{19}F noise standard deviation described above to calculate the tumor, liver, and reference tube ^{19}F signal-to-noise ratio (SNR). The ^{19}F signal, SNR and ROI volume of each animal was retained, and used together with the known reference tube concentration to calculate the tumor and liver PFC concentration. This was performed as follows: the average ^{19}F signal in the tumor or liver ROI was divided by the average ^{19}F signal in the reference tube ROI and was multiplied by the known reference tube concentration. Total amounts of tumor PFC were calculated by multiplying the PFC concentration with the PFC signal volume.

2-photon microscopy image analysis

3D-images from the high-resolution imaging of brain tumor-bearing slices were imported into Imaris version 9.7.2 (Bitplane). For each sample, 3 to 6 volumes-of-interest (VOI) were analyzed, including one VOI of the healthy contralateral brain adjacent to the tumor. Before cell/ structure classification and segmentation, images were corrected for bleed-through using the “channel arithmetic” plugin. The following signal subtractions were performed: “lectin DyLight649”-“rhodamine” to clean the lectin signal from the rhodamine bleed-through; “rhodamine”-“empty channel”, to clean the rhodamine signal from general autofluorescence. Rhodamine foci and cancer cells were classified and segmented using the “surface” creation tool. Vessels were first defined using the “surface” creation tool, and then the network composition was reconstructed with the “filament” creation tool. Vessel parameters included dendrite area, length, orientation angle, straightness, volume, diameter, ratio segments and branching points, and vessel coverage. For each VOI, vessel parameters and rhodamine-PFCE-NP uptake were Z-score normalized and the principal-component analysis (PCA) was performed using the R package “devtools”. FlowJo v10.7.1 (BD) was used to analyze single cell/foci data.

For IVM quantification, high-resolution 3D tilescan images were imported into Imaris version 9.7.2 (Bitplane). Blood vessel location was identified at the 1h time point by visualization of the circulating rhodamine-PFCE-NP, and additional landmarks were annotated (cancer cells, second harmonic generation (SHG)) to identify the same location in the timepoints 0h, 6h and 24h.

Alignment workflow of PB and IF images

IF and PB image FOVs were exported as 8-bit BigTiff files from the ZEN 2.6 blue edition software (Zeiss). Image J (National Institutes of Health, USA) was used for imaging processing. First, PB images were rescaled by a factor of 0.676923076923077 to correspond to the IF images. The Bigwarp plugin was used to align the nuclei of the IF and PB images, based on the DAPI nuclear staining and Nuclear red staining respectively, by defining at least 10 reference matching points. All channels were then concatenated, the voxel size set to 0.325x0.325 μm and a voxel depth of 2, and subsequently a hyperstack was created. All RGB channels were inverted and an ome.tif file was exported for analysis with VIS image Analysis Software (Visiopharm, see next section).

Image analysis and cell type identification

Image quantification was performed using the VIS image Analysis Software (Visiopharm). For each staining panel a specific application was designed. The tumor area was outlined based on the DAPI signal. Aberrant signals resulting from air bubbles or dust particles were manually excluded. Nuclear masks and cell marker masks were created using the application creator plugins and commands. Cell types were defined using a hierarchical decision tree based on manual thresholds of the nuclear signal and the proximity of marker masks to the nucleus. Vessels were defined based on the CD31 mask alone. “MDM-ROI” and “PB-ROI” were established by generating an ROI of 150 pixels (48.75 μm) around a positive nucleus. Cell count data and distance measurements were exported for each cell type.

Fluorescence-activated cell sorting, RNA sequencing and bioinformatics

Single cell suspensions of brain tumors were stained as indicated in the “flow cytometry” section. CD45⁺/CD11b⁺/Ly6C⁻/Ly6C⁻ rhodamine^{+/-} TAMs (>2000 cells) were sorted directly into TRIzol LS (Thermo Fischer Scientific) and immediately snap frozen in liquid nitrogen. RNA extraction, library preparation and sequencing were performed by Genewiz (South Plainfield, New Jersey, USA) on an Illumina HiSeq 2500 (Illumina). Adapter sequences and low-quality ends were removed with cutadapt, trimming for TrueSeq and polyA sequences. Reads were aligned to the mouse genome build mm10 using HISAT2 aligner. Samples were normalized with TMM method (edgeR package) and log₂ transformed with voom (limma package). Differential expression was computed with

limma, after filtering out genes with average FPKM (fragments per kilobase million) < 1. Pathway analysis was performed with mSigDB v7.0 using four collections: hallmark, canonical pathways, GO biological process and GO cellular components. Access to the data at <https://www.ncbi.nlm.nih.gov/geo/query/acc.cgi?acc=GSE190109> (token: izyhacamlhmvzkl). Publicly available raw RNA-seq data were retrieved from GEO (number GSE99537) (5).

Statistics

R version 4.1.0 was used to perform statistical analysis and graphically plot all data (ggplot package). Parametric data were analyzed by a two-tailed Student's t-test (paired or unpaired depending on the experimental setup). Non-parametric data were analyzed by a Mann-Whitney test on ranks (paired or unpaired depending on the experimental setup). $P < 0.05$ was considered as statistically significant. Each specific statistical test is reported for each experiment in the figure legends. Boxplots are used to present the data, showing median and the 25th to 75th percentiles.

Data and materials availability: The raw RNA-seq data generated in this study are accessible in the GEO under number GSE190109:

(<https://www.ncbi.nlm.nih.gov/geo/query/acc.cgi?acc=GSE190109> - provisional token: izyhacamlhmvzkl). All data associated with this study are present in the main manuscript or the Supplementary Materials.

Table 1: List of antibodies used in the study.

Target	Species	Antibodies					Application
		Antibody	Manufacturer	Clone	category number	Dilution	
Ly-6C	Rat	Anti-mouse Ly-6C Brilliant Violet 711	BioLegend	HK1.4	128037	1:800	Flow cytometry panel #1 and #3
Ly-6G	Rat	Anti-mouse Ly-6G Brilliant Violet 605	BioLegend	1A8	127639	1:160	Flow cytometry panel #1 and #3
CD11b	Rat	Anti-mouse CD11b BUV661	BD Biosciences	M1/70	612977	1:800	Flow cytometry panel #1 and #2
CD45	Rat	Anti-mouse CD45 FITC	BD Biosciences	30-F11	553080	1:200	Flow cytometry panel #1, #2 and #3
CD49d	Rat	Anti-mouse CD49d PE/Cy7	BioLegend	R1-2	103618	1:160	Flow cytometry panel #1
CD3	Hamster	Anti-mouse CD3e BUV395	BD Biosciences	145-2C11	563565	1:75	Flow cytometry panel #1 and #2
NK-1.1	Mouse	Anti-mouse NK-1.1 Brilliant Violet 421	BioLegend	PK136	108741	1:640	Flow cytometry panel #1
NK-1.1	Mouse	Anti-mouse NK-1.1 Brilliant Violet 711	BioLegend	PK136	108745	1:640	Flow cytometry panel #2
CD19	Rat	Anti-mouse CD19 Brilliant Violet 605	BioLegend	6D5	115539	1:320	Flow cytometry panel #2
CD31	Rat	Anti-mouse CD31 PE/Cy7	BioLegend	390	102418	1:100	Flow cytometry panel #2
CD11b	Rat	Anti-mouse CD11b APC	Invitrogen	M1/70	17-0112-81	1:800	Flow cytometry panel #3
CD11c	Hamster	Anti-mouse CD11c Brilliant Violet 785	BioLegend	N418	117336	1:400	Flow cytometry panel #4
CD64	Mouse	Anti-mouse CD64 FITC	BioLegend	X54-5/7.1	139316	1:320	Flow cytometry panel #4
MHCII	Rat	Anti-mouse MHCII Brilliant Violet 510	BioLegend	M5/114.15.2	107635	1:640	Flow cytometry panel #4
F4/80	Rat	Anti-mouse F4/80 Brilliant Violet 421	BioLegend	BM8	123131	1:320	Flow cytometry panel #4
CD31	Goat	Anti-mouse CD31	R&D systems	Polyclonal	AF3628	1:100	Immunofluorescence panel #1
CD68	Rat	Anti-mouse CD68	Bio-Rad	FA-11	MCA1957	1:500	Immunofluorescence panel #1
IDH2	Rabbit	Anti-mouse IDH2	Cell Signaling Technology	D8E3B	564395	1:100	Immunofluorescence panel #1
Iba1	Goat	Anti-mouse Iba1	Abcam	Polyclonal	ab5076	1:300	Immunofluorescence panel #2
P2RY12	Rabbit	Anti-mouse P2RY12	Anaspec	Polyclonal	A5-55043A	1:300	Immunofluorescence panel #2
YFP	Chicken	Anti-GFP (cross-reactive to YFP)	Abcam	Polyclonal	ab13970	1:1000	Immunofluorescence panel #3
Goat IgG (H+L)	Donkey	Anti-goat IgG Alexa Fluor 555	Invitrogen	Polyclonal	A21432	1:500	Immunofluorescence panel #1 and #2
Rabbit IgG (H+L)	Donkey	Anti-rabbit IgG Alexa Fluor 647	Invitrogen	Polyclonal	A31573	1:500	Immunofluorescence panel #1 and #2
Rat IgG (H+L)	Donkey	Anti-rat IgG DyLight 755	Invitrogen	Polyclonal	SA5-10031	1:500	Immunofluorescence panel #1
Chicken IgG (H+L)	Donkey	Anti-chicken IgG Alexa Fluor 488	Jackson ImmunoResearch	Polyclonal	703-545-155	1:500	Immunofluorescence panel #3

Flow cytometry panel #1 has been used in experiments presented in figures: 2 and S2
Flow cytometry panel #2 has been used in experiments presented in figures: 2 and S2
Flow cytometry panel #3 has been used in experiments presented in figures: 4 and S4
Flow cytometry panel #4 has been used in experiments presented in figures: 2 and S2
Immunofluorescence panel #1 has been used in experiments presented in figures: 4 and S4
Immunofluorescence panel #2 has been used in experiments presented in figures: 5, S6, S7
Immunofluorescence panel #3 has been used in experiments presented in figures: 6, 7

Funding: This research was supported in part by the Swiss Cancer Research Foundation (KFS-3390-08-2016; KFS-5280-02-2021), Charlie Teo Foundation, Ludwig Institute for Cancer Research, and University of Lausanne (to JAJ), the Swiss National Science Foundation (32003B_182615 to RBvH), the Deutsche Forschungsgemeinschaft (TE1209/1-1 & 1-2; FL303; to ST and UF), the E. Schrödinger fellowship J4343 by the Austrian Science Fund FWF (to KS), a Human Frontier Science Program fellowship (LT000240/2017-L), a Veni fellowship from the Netherlands Organization for Scientific Research (09150161910076) (to AZ), and the European Union's Horizon 2020 research and innovation program under the Marie Skłodowska–Curie grant agreement (No. 955951, Evomet ITN), which supports R.S.M.

Author contributions: D.C., R.B.v.H. and J.A.J. conceived the study, designed experiments, and interpreted data. D.C. and J.A.J. wrote the manuscript. D.C., R.S.M., K.S., A.Z., R.C., V.W., and R.B.v.H. performed the experiments. S.T. and U.F. provided materials. D.C. and R.B.v.H.

performed the MRI analyses, N.F. performed the RNA-seq analyses, D.C. performed all other experimental analyses. All authors edited or commented on the manuscript.

Competing interests: The authors declare that they have no competing interests.

Acknowledgments: We thank members of the Joyce lab for insightful discussion, and Matteo Massara, Lucie Tillard, Mara Kornete and Simone Rumac for excellent technical support. We are grateful to the In Vivo Imaging Facility and the Flow Cytometry Facility at the University of Lausanne for assistance and advice, in particular Alexandre Benechet and Danny Labes respectively. We thank Leila Akkari, NKI, and Ping-Chih Ho, UNIL, for informative scientific discussions. We also acknowledge the CIBM Center for Biomedical Imaging, founded and supported by Lausanne University Hospital (CHUV), University of Lausanne (UNIL), École Polytechnique Fédérale de Lausanne (EPFL), University of Geneva (UNIGE) and Geneva University Hospitals (HUG).

References and Notes

1. D. F. Quail, J. A. Joyce, The Microenvironmental Landscape of Brain Tumors. *Cancer Cell* 31, 326-341 (2017).
2. B. M. Andersen, C. Faust Akl, M. A. Wheeler, E. A. Chiocca, D. A. Reardon, F. J. Quintana, Glial and myeloid heterogeneity in the brain tumour microenvironment. *Nat Rev Cancer* 21, 786-802 (2021).
3. F. Klemm, R. R. Maas, R. L. Bowman, M. Kornete, K. Soukup, S. Nassiri, J. P. Brouland, C. A. Iacobuzio-Donahue, C. Brennan, V. Tabar, P. H. Gutin, R. T. Daniel, M. E. Hegi, J. A. Joyce, Interrogation of the Microenvironmental Landscape in Brain Tumors Reveals Disease-Specific Alterations of Immune Cells. *Cell* 181, 1643-1660 e1617 (2020).
4. E. Friebel, K. Kapolou, S. Unger, N. G. Nunez, S. Utz, E. J. Rushing, L. Regli, M. Weller, M. Greter, S. Tugues, M. C. Neidert, B. Becher, Single-Cell Mapping of Human Brain Cancer Reveals Tumor-Specific Instruction of Tissue-Invading Leukocytes. *Cell* 181, 1626-1642 e1620 (2020).
5. L. Akkari, R. L. Bowman, J. Tessier, F. Klemm, S. M. Handgraaf, M. de Groot, D. F. Quail, L. Tillard, J. Gadiot, J. T. Huse, D. Brandsma, J. Westerga, C. Watts, J. A. Joyce, Dynamic changes in glioma macrophage populations after radiotherapy reveal CSF-1R inhibition as a strategy to overcome resistance. *Sci Transl Med* 12, eaaw7843 (2020).
6. D. N. Louis, A. Perry, P. Wesseling, D. J. Brat, I. A. Cree, D. Figarella-Branger, C. Hawkins, H. K. Ng, S. M. Pfister, G. Reifenberger, R. Soffietti, A. von Deimling, D. W. Ellison, The 2021 WHO Classification of Tumors of the Central Nervous System: a summary. *Neuro Oncol* 23, 1231-1251 (2021).
7. R. Stupp, W. P. Mason, M. J. van den Bent, M. Weller, B. Fisher, M. J. Taphoorn, K. Belanger, A. A. Brandes, C. Marosi, U. Bogdahn, J. Curschmann, R. C. Janzer, S. K. Ludwin, T. Gorlia, A. Allgeier, D. Lacombe, J. G. Cairncross, E. Eisenhauer, R. O. Mirimanoff, R. European Organisation for, T. Treatment of Cancer Brain, G. Radiotherapy, G. National Cancer Institute of Canada Clinical Trials, Radiotherapy plus concomitant and adjuvant temozolomide for glioblastoma. *N Engl J Med* 352, 987-996 (2005).
8. P. Magod, I. Mastandrea, L. Rousso-Noori, L. Agemy, G. Shapira, N. Shomron, D. Friedmann-Morvinski, Exploring the longitudinal glioma microenvironment landscape uncovers reprogrammed pro-tumorigenic neutrophils in the bone marrow. *Cell Rep* 36, 109480 (2021).
9. J. Kowal, M. Kornete, J. A. Joyce, Re-education of macrophages as a therapeutic strategy in cancer. *Immunotherapy* 11, 677-689 (2019).
10. S. M. Pyonteck, L. Akkari, A. J. Schuhmacher, R. L. Bowman, L. Sevenich, D. F. Quail, O. C. Olson, M. L. Quick, J. T. Huse, V. Teijeiro, M. Setty, C. S. Leslie, Y. Oei, A. Pedraza, J. Zhang, C. W. Brennan, J. C. Sutton, E. C. Holland, D. Daniel, J. A. Joyce, CSF-1R inhibition alters macrophage polarization and blocks glioma progression. *Nat Med* 19, 1264-1272 (2013).
11. D. F. Quail, R. L. Bowman, L. Akkari, M. L. Quick, A. J. Schuhmacher, J. T. Huse, E. C. Holland, J. C. Sutton, J. A. Joyce, The tumor microenvironment underlies acquired resistance to CSF-1R inhibition in gliomas. *Science* 352, aad3018 (2016).
12. D. Yan, J. Kowal, L. Akkari, A. J. Schuhmacher, J. T. Huse, B. L. West, J. A. Joyce, Inhibition of colony stimulating factor-1 receptor abrogates microenvironment-mediated therapeutic resistance in gliomas. *Oncogene* 36, 6049-6058 (2017).
13. I. L. Tan, R. D. N. Arifa, H. Rallapalli, V. Kana, Z. Lao, R. M. Sanghrajka, N. Sumru Bayin, A. Tanne, A. Wojcinski, A. Korshunov, N. Bhardwaj, M. Merad, D. H. Turnbull, J.

- J. Lafaille, A. L. Joyner, CSF1R inhibition depletes tumor-associated macrophages and attenuates tumor progression in a mouse sonic Hedgehog-Medulloblastoma model. *Oncogene* 40, 396-407 (2021).
14. F. Klemm, A. Möckl, A. Salamero-Boix, T. Alekseeva, A. Schaffer, M. Schulz, K. Niesel, R. R. Maas, M. Groth, B. T. Elie, R. L. Bowman, M. E. Hegi, R. T. Daniel, P. S. Zeiner, J. Zinke, P. N. Harter, K. H. Plate, J. A. Joyce, L. Sevenich, Compensatory CSF2-driven macrophage activation promotes adaptive resistance to CSF1R inhibition in breast-to-brain metastasis. *Nat Cancer* 2, 1086-1101 (2021).
 15. M. G.-M. C. Lin, T. M. Bauer, A. Naing, D. Wan-Teck Lim, J. Sarantopoulos, R. Geva, Y. Ando, L. Fan, S. Choudhury, P. Tu, C. Quadt, A. Santoro. , Phase I study of BLZ945 alone and with spartalizumab (PDR001) in patients (pts) with advanced solid tumors [abstract]. *Cancer Res* 80, (2020).
 16. M. Smits, MRI biomarkers in neuro-oncology. *Nat Rev Neurol* 17, 486-500 (2021).
 17. H. Mehrabian, J. Detsky, H. Soliman, A. Sahgal, G. J. Stanisz, Advanced Magnetic Resonance Imaging Techniques in Management of Brain Metastases. *Front Oncol* 9, 440 (2019).
 18. Q. Li, F. Dong, B. Jiang, M. Zhang, Exploring MRI Characteristics of Brain Diffuse Midline Gliomas With the H3 K27M Mutation Using Radiomics. *Front Oncol* 11, 646267 (2021).
 19. D. Li, C. B. Patel, G. Xu, A. Iagaru, Z. Zhu, L. Zhang, Z. Cheng, Visualization of Diagnostic and Therapeutic Targets in Glioma With Molecular Imaging. *Front Immunol* 11, 592389 (2020).
 20. S. Mukherjee, D. Sonanini, A. Maurer, H. E. Daldrup-Link, The yin and yang of imaging tumor associated macrophages with PET and MRI. *Theranostics* 9, 7730-7748 (2019).
 21. R. Weissleder, M. Nahrendorf, M. J. Pittet, Imaging macrophages with nanoparticles. *Nat Mater* 13, 125-138 (2014).
 22. C. Jacoby, S. Temme, F. Mayenfels, N. Benoit, M. P. Krafft, R. Schubert, J. Schrader, U. Fogel, Probing different perfluorocarbons for in vivo inflammation imaging by ¹⁹F MRI: image reconstruction, biological half-lives and sensitivity. *NMR Biomed* 27, 261-271 (2014).
 23. E. Darcot, R. Colotti, D. Brennan, G. A. Deuchar, C. Santosh, R. B. van Heeswijk, A characterization of ABL-101 as a potential tracer for clinical fluorine-19 MRI. *NMR Biomed* 33, e4212 (2020).
 24. U. Fogel, Z. Ding, H. Hardung, S. Jander, G. Reichmann, C. Jacoby, R. Schubert, J. Schrader, In vivo monitoring of inflammation after cardiac and cerebral ischemia by fluorine magnetic resonance imaging. *Circulation* 118, 140-148 (2008).
 25. R. B. van Heeswijk, M. Pellegrin, U. Fogel, C. Gonzales, J. F. Aubert, L. Mazzolai, J. Schwitter, M. Stuber, Fluorine MR Imaging of Inflammation in Atherosclerotic Plaque in Vivo. *Radiology* 275, 421-429 (2015).
 26. F. Nienhaus, D. Colley, A. Jahn, S. Pfeiler, V. Flocke, S. Temme, M. Kelm, N. Gerdes, U. Fogel, F. Bonner, Phagocytosis of a PFOB-Nanoemulsion for (¹⁹F) Magnetic Resonance Imaging: First Results in Monocytes of Patients with Stable Coronary Artery Disease and ST-Elevation Myocardial Infarction. *Molecules* 24, 2058 (2019).
 27. E. T. Ahrens, R. Flores, H. Xu, P. A. Morel, in *Nat Biotechnol.* (2005), vol. 23, pp. 983-987.
 28. D. Hambardzumyan, N. M. Amankulor, K. Y. Helmy, O. J. Becher, E. C. Holland, Modeling Adult Gliomas Using RCAS/t-va Technology. *Transl Oncol* 2, 89-95 (2009).
 29. R. L. Bowman, F. Klemm, L. Akkari, S. M. Pyonteck, L. Sevenich, D. F. Quail, S. Dhara, K. Simpson, E. E. Gardner, C. A. Iacobuzio-Donahue, C. W. Brennan, V. Tabar, P. H.

- Gutin, J. A. Joyce, Macrophage Ontogeny Underlies Differences in Tumor-Specific Education in Brain Malignancies. *Cell Rep* 17, 2445-2459 (2016).
30. C. J. Herting, Z. Chen, V. Maximov, A. Duffy, F. Szulzewsky, D. M. Shayakhmetov, D. Hambardzumyan, Tumour-associated macrophage-derived interleukin-1 mediates glioblastoma-associated cerebral oedema. *Brain* 142, 3834-3851 (2019).
 31. A. Di Costanzo, T. Scarabino, F. Trojsi, T. Popolizio, D. Catapano, G. M. Giannatempo, S. Bonavita, M. Portaluri, M. Tosetti, V. A. d'Angelo, U. Salvolini, G. Tedeschi, Proton MR spectroscopy of cerebral gliomas at 3 T: spatial heterogeneity, and tumour grade and extent. *Eur Radiol* 18, 1727-1735 (2008).
 32. M. N. Hasan, L. Luo, D. Ding, S. Song, M. I. H. Bhuiyan, R. Liu, L. M. Foley, X. Guan, G. Kohanbash, T. K. Hitchens, M. G. Castro, Z. Zhang, D. Sun, Blocking NHE1 stimulates glioma tumor immunity by restoring OXPHOS function of myeloid cells. *Theranostics* 11, 1295-1309 (2021).
 33. A. V. Makela, J. M. Gaudet, P. J. Foster, Quantifying tumor associated macrophages in breast cancer: a comparison of iron and fluorine-based MRI cell tracking. *Sci Rep* 7, 42109 (2017).
 34. A. V. Makela, P. J. Foster, Imaging macrophage distribution and density in mammary tumors and lung metastases using fluorine-19 MRI cell tracking. *Magn Reson Med* 80, 1138-1147 (2018).
 35. O. C. Olson, H. Kim, D. F. Quail, E. A. Foley, J. A. Joyce, Tumor-Associated Macrophages Suppress the Cytotoxic Activity of Antimitotic Agents. *Cell Rep* 19, 101-113 (2017).
 36. A. Leftin, N. Ben-Chetrit, J. A. Joyce, J. A. Koutcher, Imaging endogenous macrophage iron deposits reveals a metabolic biomarker of polarized tumor macrophage infiltration and response to CSF1R breast cancer immunotherapy. *Sci Rep* 9, 857 (2019).
 37. A. Khurana, F. Chapelin, H. Xu, J. R. Acevedo, A. Molinolo, Q. Nguyen, E. T. Ahrens, Visualization of macrophage recruitment in head and neck carcinoma model using fluorine-19 magnetic resonance imaging. *Magn Reson Med* 79, 1972-1980 (2018).
 38. A. R. Pombo Antunes, I. Scheyltjens, F. Lodi, J. Messiaen, A. Antoranz, J. Duerinck, D. Kancheva, L. Martens, K. De Vlaminck, H. Van Hove, S. S. Kjolner Hansen, F. M. Bosisio, K. Van der Borcht, S. De Vleeschouwer, R. Sciot, L. Bouwens, M. Verfaillie, N. Vandamme, R. E. Vandenbroucke, O. De Wever, Y. Saeys, M. Guilliams, C. Gysemans, B. Neyns, F. De Smet, D. Lambrechts, J. A. Van Ginderachter, K. Movahedi, Single-cell profiling of myeloid cells in glioblastoma across species and disease stage reveals macrophage competition and specialization. *Nat Neurosci* 24, 595-610 (2021).
 39. C. D. Arvanitis, G. B. Ferraro, R. K. Jain, The blood-brain barrier and blood-tumour barrier in brain tumours and metastases. *Nat Rev Cancer* 20, 26-41 (2020).
 40. P. Bouvain, V. Flocke, W. Kramer, R. Schubert, J. Schrader, U. Flogel, S. Temme, Dissociation of (19)F and fluorescence signal upon cellular uptake of dual-contrast perfluorocarbon nanoemulsions. *MAGMA* 32, 133-145 (2019).
 41. A. Zomer, D. Croci, J. Kowal, L. van Gurp, J. A. Joyce, Multimodal imaging of the dynamic brain tumor microenvironment during glioblastoma progression and in response to treatment. *iScience* 25, 104570 (2022).
 42. C. Carmona-Fontaine, M. Deforet, L. Akkari, C. B. Thompson, J. A. Joyce, J. B. Xavier, Metabolic origins of spatial organization in the tumor microenvironment. *Proc Natl Acad Sci U S A* 114, 2934-2939 (2017).
 43. C. N. Parkhurst, G. Yang, I. Ninan, J. N. Savas, J. R. Yates, 3rd, J. J. Lafaille, B. L. Hempstead, D. R. Littman, W. B. Gan, Microglia promote learning-dependent synapse formation through brain-derived neurotrophic factor. *Cell* 155, 1596-1609 (2013).

44. C. Chirizzi, D. De Battista, I. Tirodda, P. Metrangolo, G. Comi, F. B. Bombelli, L. Chaabane, Multispectral MRI with Dual Fluorinated Probes to Track Mononuclear Cell Activity in Mice. *Radiology* 291, 351-357 (2019).
45. U. Flogel, S. Temme, C. Jacoby, T. Oerther, P. Keul, V. Flocke, X. Wang, F. Bonner, F. Nienhaus, K. Peter, J. Schrader, M. Grandoch, M. Kelm, B. Levkau, Multi-targeted (1)H/(19)F MRI unmasks specific danger patterns for emerging cardiovascular disorders. *Nat Commun* 12, 5847 (2021).
46. M. Puchala, Z. Szweda-Lewandowska, J. Kiefer, The influence of radiation quality on radiation-induced hemolysis and hemoglobin oxidation of human erythrocytes. *J Radiat Res* 45, 275-279 (2004).
47. W. B. Rittase, J. M. Muir, J. E. Slaven, R. M. Bouten, M. A. Bylicky, W. L. Wilkins, R. M. Day, Deposition of Iron in the Bone Marrow of a Murine Model of Hematopoietic Acute Radiation Syndrome. *Exp Hematol* 84, 54-66 (2020).
48. K. Zormpas-Petridis, N. P. Jerome, M. D. Blackledge, F. Carceller, E. Poon, M. Clarke, C. M. McErlean, G. Barone, A. Koers, S. J. Vaidya, L. V. Marshall, A. D. J. Pearson, L. Moreno, J. Anderson, N. Sebire, K. McHugh, D. M. Koh, Y. Yuan, L. Chesler, S. P. Robinson, Y. Jamin, MRI Imaging of the Hemodynamic Vasculature of Neuroblastoma Predicts Response to Antiangiogenic Treatment. *Cancer Res* 79, 2978-2991 (2019).
49. H. G. Wirsching, U. Roelcke, J. Weller, T. Hundsberger, A. F. Hottinger, R. von Moos, F. Caparrotti, K. Conen, L. Remonda, P. Roth, A. Ochsenbein, G. Tabatabai, M. Weller, MRI and (18)FET-PET Predict Survival Benefit from Bevacizumab Plus Radiotherapy in Patients with Isocitrate Dehydrogenase Wild-type Glioblastoma: Results from the Randomized ARTE Trial. *Clin Cancer Res* 27, 179-188 (2021).
50. I. Dregely, D. Prezzi, C. Kelly-Morland, E. Roccia, R. Neji, V. Goh, Imaging biomarkers in oncology: Basics and application to MRI. *J Magn Reson Imaging* 48, 13-26 (2018).
51. M. C. Ku, S. Waiczies, T. Niendorf, A. Pohlmann, Assessment of Blood Brain Barrier Leakage with Gadolinium-Enhanced MRI. *Methods Mol Biol* 1718, 395-408 (2018).
52. M. Molgora, M. Colonna, Turning enemies into allies-reprogramming tumor-associated macrophages for cancer therapy. *Med (N Y)* 2, 666-681 (2021).
53. M. Gromeier, M. C. Brown, G. Zhang, X. Lin, Y. Chen, Z. Wei, N. Beaubier, H. Yan, Y. He, A. Desjardins, J. E. Herndon, 2nd, F. S. Varn, R. G. Verhaak, J. Zhao, D. P. Bolognesi, A. H. Friedman, H. S. Friedman, F. McSherry, A. M. Muscat, E. S. Lipp, S. K. Nair, M. Khasraw, K. B. Peters, D. Randazzo, J. H. Sampson, R. E. McLendon, D. D. Bigner, D. M. Ashley, Very low mutation burden is a feature of inflamed recurrent glioblastomas responsive to cancer immunotherapy. *Nat Commun* 12, 352 (2021).
54. N. C. Swinburne, J. Schefflein, Y. Sakai, E. K. Oermann, J. J. Titano, I. Chen, S. Tadayon, A. Aggarwal, A. Doshi, K. Nael, Machine learning for semi-automated classification of glioblastoma, brain metastasis and central nervous system lymphoma using magnetic resonance advanced imaging. *Ann Transl Med* 7, 232 (2019).
55. K. Niesel, M. Schulz, J. Anthes, T. Alekseeva, J. Macas, A. Salamero-Boix, A. Mockl, T. Oberwahrenbrock, M. Lohies, S. Stein, K. H. Plate, Y. Reiss, F. Rodel, L. Sevenich, The immune suppressive microenvironment affects efficacy of radio-immunotherapy in brain metastasis. *EMBO Mol Med* 13, e13412 (2021).
56. C. Gonzales, H. A. Yoshihara, N. Dilek, J. Leignadier, M. Irving, P. Mievil, L. Helm, O. Michielin, J. Schwitter, In-Vivo Detection and Tracking of T Cells in Various Organs in a Melanoma Tumor Model by 19F-Fluorine MRS/MRI. *PLoS One* 11, e0164557 (2016).
57. E. T. Ahrens, B. M. Helfer, C. F. O'Hanlon, C. Schirda, Clinical cell therapy imaging using a perfluorocarbon tracer and fluorine-19 MRI. *Magn Reson Med* 72, 1696-1701 (2014).

58. S. Weibel, T. C. Basse-Luesebrink, M. Hess, E. Hofmann, C. Seubert, J. Langbein-Laugwitz, I. Gentshev, V. J. Sturm, Y. Ye, T. Kampf, P. M. Jakob, A. A. Szalay, Imaging of intratumoral inflammation during oncolytic virotherapy of tumors by ¹⁹F-magnetic resonance imaging (MRI). *PLoS One* 8, e56317 (2013).
59. R. B. van Heeswijk, J. De Blois, G. Kania, C. Gonzales, P. Blyszczuk, M. Stuber, U. Eriksson, J. Schwitter, Selective in vivo visualization of immune-cell infiltration in a mouse model of autoimmune myocarditis by fluorine-19 cardiac magnetic resonance. *Circ Cardiovasc Imaging* 6, 277-284 (2013).
60. E. Darcot, R. Colotti, M. Pellegrin, A. Wilson, S. Siegert, K. Bouzourene, J. Yerly, L. Mazzolai, M. Stuber, R. B. van Heeswijk, Towards Quantification of Inflammation in Atherosclerotic Plaque in the Clinic - Characterization and Optimization of Fluorine-19 MRI in Mice at 3 T. *Sci Rep* 9, 17488 (2019).
61. A. Balducci, Y. Wen, Y. Zhang, B. M. Helfer, T. K. Hitchens, W. S. Meng, A. K. Wesa, J. M. Janjic, A novel probe for the non-invasive detection of tumor-associated inflammation. *Oncoimmunology* 2, e23034 (2013).
62. L. Alvaro-Espinosa, A. de Pablos-Aragoneses, M. Valiente, N. Priego, Brain Microenvironment Heterogeneity: Potential Value for Brain Tumors. *Front Oncol* 11, 714428 (2021).
63. A. A. Mohan, W. H. Tomaszewski, A. P. Haskell-Mendoza, K. M. Hotchkiss, K. Singh, J. L. Reedy, P. E. Fecci, J. H. Sampson, M. Khasraw, Targeting Immunometabolism in Glioblastoma. *Front Oncol* 11, 696402 (2021).
64. S. K. Wculek, G. Dunphy, I. Heras-Murillo, A. Mastrangelo, D. Sancho, Metabolism of tissue macrophages in homeostasis and pathology. *Cell Mol Immunol* 19, 384-408 (2021).
65. M. L. Squadrito, F. Pucci, L. Magri, D. Moi, G. D. Gilfillan, A. Raghetti, A. Casazza, M. Mazzone, R. Lyle, L. Naldini, M. De Palma, miR-511-3p modulates genetic programs of tumor-associated macrophages. *Cell Rep* 1, 141-154 (2012).
66. C. Baer, M. L. Squadrito, D. Laoui, D. Thompson, S. K. Hansen, A. Kiialainen, S. Hoves, C. H. Ries, C. H. Ooi, M. De Palma, Suppression of microRNA activity amplifies IFN-gamma-induced macrophage activation and promotes anti-tumour immunity. *Nat Cell Biol* 18, 790-802 (2016).
67. S. C. Huang, B. Everts, Y. Ivanova, D. O'Sullivan, M. Nascimento, A. M. Smith, W. Beatty, L. Love-Gregory, W. Y. Lam, C. M. O'Neill, C. Yan, H. Du, N. A. Abumrad, J. F. Urban, Jr., M. N. Artyomov, E. L. Pearce, E. J. Pearce, Cell-intrinsic lysosomal lipolysis is essential for alternative activation of macrophages. *Nat Immunol* 15, 846-855 (2014).
68. P. J. Coates, J. K. Rundle, S. A. Lorimore, E. G. Wright, Indirect macrophage responses to ionizing radiation: implications for genotype-dependent bystander signaling. *Cancer Res* 68, 450-456 (2008).
69. F. O. Martinez, S. Gordon, M. Locati, A. Mantovani, Transcriptional profiling of the human monocyte-to-macrophage differentiation and polarization: new molecules and patterns of gene expression. *J Immunol* 177, 7303-7311 (2006).
70. K. Kierdorf, T. Masuda, M. J. C. Jordao, M. Prinz, Macrophages at CNS interfaces: ontogeny and function in health and disease. *Nat Rev Neurosci* 20, 547-562 (2019).
71. A. Moore, R. Weissleder, A. Bogdanov, Jr., Uptake of dextran-coated monocrystalline iron oxides in tumor cells and macrophages. *J Magn Reson Imaging* 7, 1140-1145 (1997).
72. C. Zimmer, S. C. Wright, Jr., R. T. Engelhardt, G. A. Johnson, C. Kramm, X. O. Breakefield, R. Weissleder, Tumor cell endocytosis imaging facilitates delineation of the glioma-brain interface. *Exp Neurol* 143, 61-69 (1997).

73. H. Konishi, T. Okamoto, Y. Hara, O. Komine, H. Tamada, M. Maeda, F. Osako, M. Kobayashi, A. Nishiyama, Y. Kataoka, T. Takai, N. Udagawa, S. Jung, K. Ozato, T. Tamura, M. Tsuda, K. Yamanaka, T. Ogi, K. Sato, H. Kiyama, Astrocytic phagocytosis is a compensatory mechanism for microglial dysfunction. *EMBO J* 39, e104464 (2020).
74. B. Zhang, C. Gaiteri, L. G. Bodea, Z. Wang, J. McElwee, A. A. Podtelezchnikov, C. Zhang, T. Xie, L. Tran, R. Dobrin, E. Fluder, B. Clurman, S. Melquist, M. Narayanan, C. Suver, H. Shah, M. Mahajan, T. Gillis, J. Mysore, M. E. MacDonald, J. R. Lamb, D. A. Bennett, C. Molony, D. J. Stone, V. Gudnason, A. J. Myers, E. E. Schadt, H. Neumann, J. Zhu, V. Emilsson, Integrated systems approach identifies genetic nodes and networks in late-onset Alzheimer's disease. *Cell* 153, 707-720 (2013).
75. A. DeRosa, A. Leftin, The Iron Curtain: Macrophages at the Interface of Systemic and Microenvironmental Iron Metabolism and Immune Response in Cancer. *Front Immunol* 12, 614294 (2021).
76. M. A. Miller, S. Arlauckas, R. Weissleder, Prediction of Anti-cancer Nanotherapy Efficacy by Imaging. *Nanotheranostics* 1, 296-312 (2017).
77. T. Mathivet, C. Bouleti, M. Van Woensel, F. Stanchi, T. Verschuere, L. K. Phng, J. Dejaegher, M. Balcer, K. Matsumoto, P. B. Georgieva, J. Belmans, R. Sciot, C. Stockmann, M. Mazzone, S. De Vleeschouwer, H. Gerhardt, Dynamic stroma reorganization drives blood vessel dysmorphia during glioma growth. *EMBO Mol Med* 9, 1629-1645 (2017).
78. T. N. Phoenix, D. M. Patmore, S. Boop, N. Boulos, M. O. Jacus, Y. T. Patel, M. F. Roussel, D. Finkelstein, L. Goumnerova, S. Perreault, E. Wadhwa, Y. J. Cho, C. F. Stewart, R. J. Gilbertson, Medulloblastoma Genotype Dictates Blood Brain Barrier Phenotype. *Cancer Cell* 29, 508-522 (2016).
79. K. M. Sullivan, A. Dean, M. M. Soe, OpenEpi: a web-based epidemiologic and statistical calculator for public health. *Public Health Rep* 124, 471-474 (2009).
80. C. Dai, J. C. Celestino, Y. Okada, D. N. Louis, G. N. Fuller, E. C. Holland, PDGF autocrine stimulation dedifferentiates cultured astrocytes and induces oligodendrogliomas and oligoastrocytomas from neural progenitors and astrocytes in vivo. *Genes Dev* 15, 1913-1925 (2001).
81. T. Ozawa, M. Riester, Y. K. Cheng, J. T. Huse, M. Squatrito, K. Helmy, N. Charles, F. Michor, E. C. Holland, Most human non-GCIMP glioblastoma subtypes evolve from a common proneural-like precursor glioma. *Cancer Cell* 26, 288-300 (2014).
82. D. F. Quail, O. C. Olson, P. Bhardwaj, L. A. Walsh, L. Akkari, M. L. Quick, I. C. Chen, N. Wendel, N. Ben-Chetrit, J. Walker, P. R. Holt, A. J. Dannenberg, J. A. Joyce, Obesity alters the lung myeloid cell landscape to enhance breast cancer metastasis through IL5 and GM-CSF. *Nat Cell Biol* 19, 974-987 (2017).
83. L. Sevenich, R. L. Bowman, S. D. Mason, D. F. Quail, F. Rapaport, B. T. Elie, E. Brogi, P. K. Brastianos, W. C. Hahn, L. J. Holsinger, J. Massague, C. S. Leslie, J. A. Joyce, Analysis of tumour- and stroma-supplied proteolytic networks reveals a brain-metastasis-promoting role for cathepsin S. *Nat Cell Biol* 16, 876-888 (2014).
84. W. H. Chae, K. Niesel, M. Schulz, F. Klemm, J. A. Joyce, M. Prummer, B. Brill, J. Bergs, F. Rodel, U. Pilatus, L. Sevenich, Evaluating Magnetic Resonance Spectroscopy as a Tool for Monitoring Therapeutic Response of Whole Brain Radiotherapy in a Mouse Model for Breast-to-Brain Metastasis. *Front Oncol* 9, 1324 (2019).
85. R. Colotti, J. A. M. Bastiaansen, A. Wilson, U. Flogel, C. Gonzales, J. Schwitter, M. Stuber, R. B. van Heeswijk, Characterization of perfluorocarbon relaxation times and their influence on the optimization of fluorine-19 MRI at 3 tesla. *Magn Reson Med* 77, 2263-2271 (2017).

86. R. Watts, Y. Wang, k-space interpretation of the Rose Model: noise limitation on the detectable resolution in MRI. *Magn Reson Med* 48, 550-554 (2002).

Figures

Fig. 1

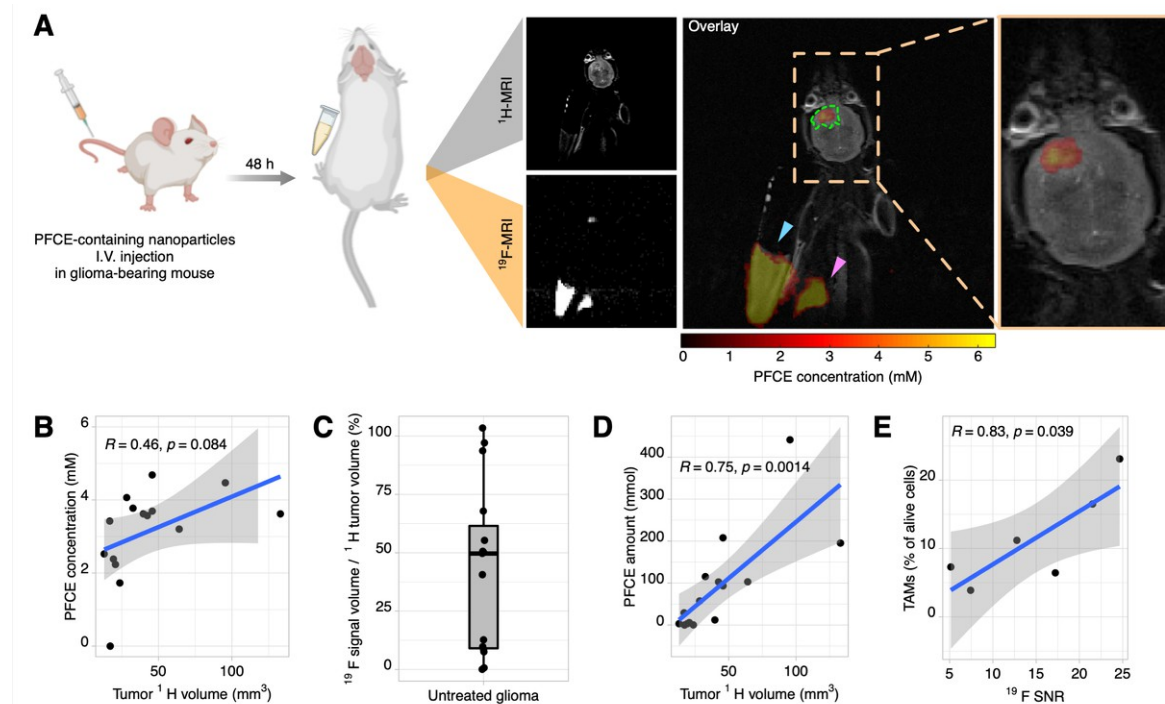


Fig. 1. ^{19}F MRI allows the non-invasive imaging of glioma-associated inflammation. **(A)** ^{19}F MR imaging workflow: PDG-Ink4a/Arf KO glioma-bearing mice were injected with perfluoro-crown-ether-containing nanoparticles (PFCE-NP) and then imaged 48h later by conventional ^1H MRI to visualize the anatomical location of the tumor, in addition to molecular ^{19}F MRI. The overlay (right) shows the ^{19}F signal evident in the tumor (dashed green line), but not in the contralateral healthy brain, in the liver (pink arrow) and in a PFCE-NP-containing reference tube (cyan arrow) placed adjacent to the mouse, which allows the absolute quantification of the tumor signal into a PFCE amount/concentration. Imaging was performed using a clinical 3T MRI scanner (Prisma, Siemens) at the local hospital (Lausanne University Hospital (CHUV), Lausanne). **(B)** Correlation of the PFCE concentration and ^1H tumor volume. **(C)** Percentage of ^{19}F signal coverage of the total tumor ^1H volume. **(D)** Correlation of the total PFCE amount and ^1H tumor volume. **(E)** Correlation of the ^{19}F signal-to-noise ratio (SNR) with the abundance of tumor-associated macrophages (TAMs) (CD45 $^+$ CD11b $^+$ Ly6G $^-$ Ly6C $^-$) quantified by flow cytometry (FCM). Mouse silhouette, syringe and reference tube drawings in (A) were sourced from <https://app.biorender.com/biorender-templates>. PDG-Ink4a/Arf KO model: n=15 mice. Regression analysis: linear model.

Fig. 2

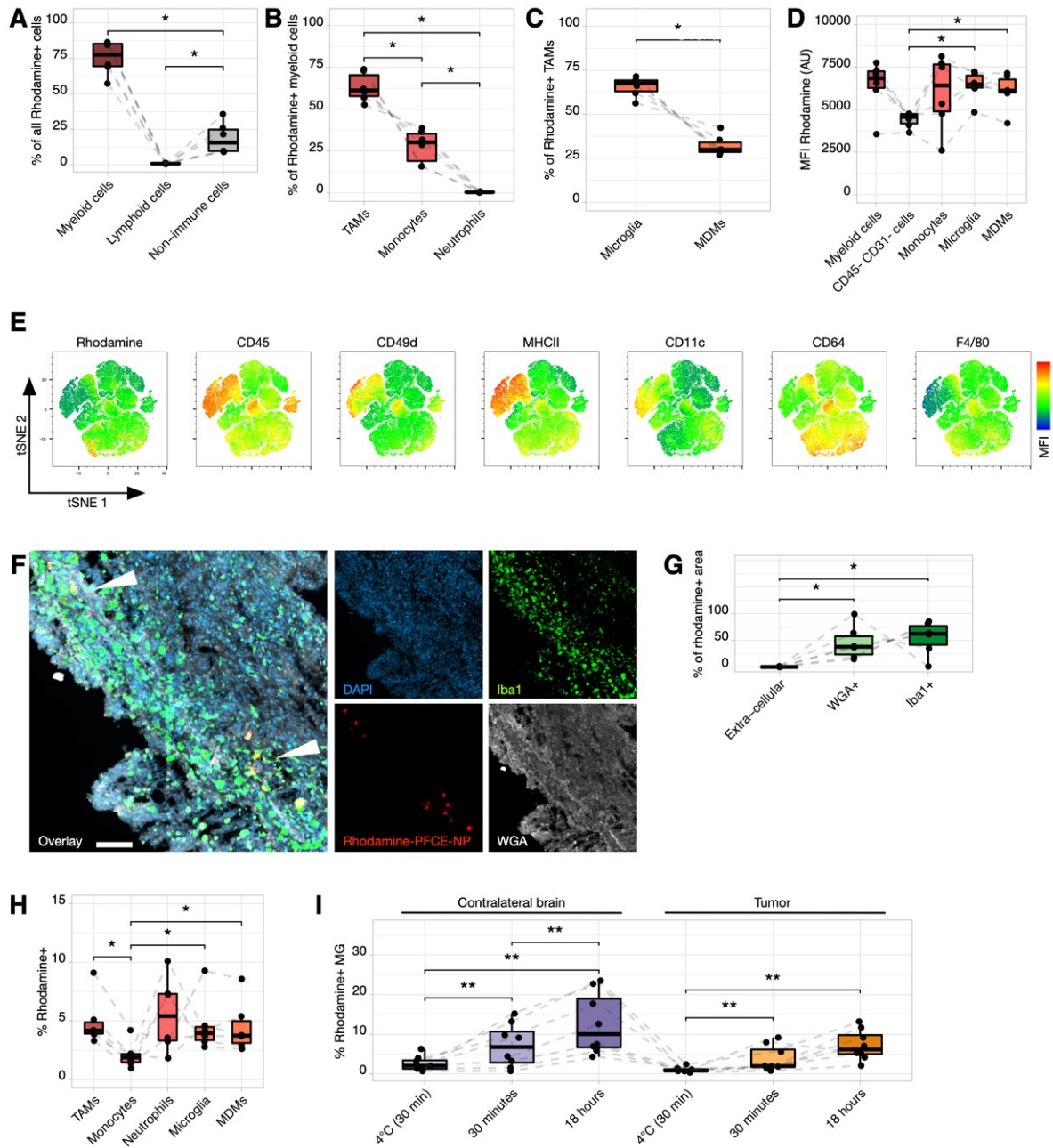


Fig. 2. PFCE-NP cellular accumulation predominantly occurs in the TAM compartment. **(A)** Flow cytometry characterization of the fluorescent rhodamine-labelled PFCE-NP positive (rhodamine-PFCE-NP+) cell pool in PDG-Ink4a/Arf KO gliomas, showing a higher proportion of the myeloid compartment (CD45+ CD11b+ cells) than non-immune cells (CD45- CD11b-) and lymphoid cells (CD45+ CD11b-). n=6 mice. **(B)** Depiction of all rhodamine-PFCE-NP+ myeloid cells showing tumor-associated macrophages (TAMs) (CD45+ CD11b+ Ly6G- Ly6C-), monocytes (CD45+ CD11b+ Ly6G+ Ly6C+) and neutrophils (CD45+ CD11b+ Ly6G+ Ly6C+). n=6 mice. **(C)** Delineation of rhodamine-PFCE-NP+ TAMs between microglia (MG) (CD49d-) and monocyte-

derived macrophages (MDMs) (CD49d⁺). n=6 mice. **(D)** Median fluorescence intensity (MFI) of the rhodamine signal in the different myeloid cell types and CD45⁻ CD31⁻ cells. n=6 mice. **(E)** t-distributed stochastic neighbor embedding (tSNE) analysis of TAMs (CD45⁺ CD11b⁺ Ly6G⁻ Ly6C⁻). FCM data showing the expression of different cell surface markers. The tSNE analysis was based on the markers CD45, CD11b, Ly6G, Ly6C, CD49d, MHCII, CD11c, CD64, and F4/80. n=6 mice, pooled. **(F)** Representative immunofluorescence (IF) image of glioma tissue showing DAPI-labelled cell nuclei (blue), the pan-macrophage marker Iba1 (green), rhodamine-PFCE-NP (red) and cell membrane staining with wheat germ agglutinin (WGA – white). White arrows indicate double positive Iba1/rhodamine-PFCE-NP cells. Scale bar: 100 μ m. **(G)** Quantification of the IF images showing the percentage of the total rhodamine⁺ area in each cellular and non-cellular compartment. n=6 mice. **(H)** Quantification of the percentage of rhodamine-PFCE-NP⁺ cells in the different myeloid populations. n=6 mice. **(I)** Quantification of rhodamine-PFCE-NP⁺ MG (CD45⁺ CD11b⁺ Ly6G⁻ Ly6C⁻ CD49d⁻) after *ex vivo* treatment of dissociated contralateral brains and matched tumors. n=8 mice. **(J)** Quantification of rhodamine-PFCE-NP⁺ MG (CD45⁺ CD11b⁺ Ly6G⁻ Ly6C⁻ CD49d⁻) after *ex vivo* treatment of dissociated contralateral brains and matched tumors. n=8 mice. * P<0.05, ** P<0.01, not significant if not otherwise stated, paired Wilcoxon test.

Fig. 3

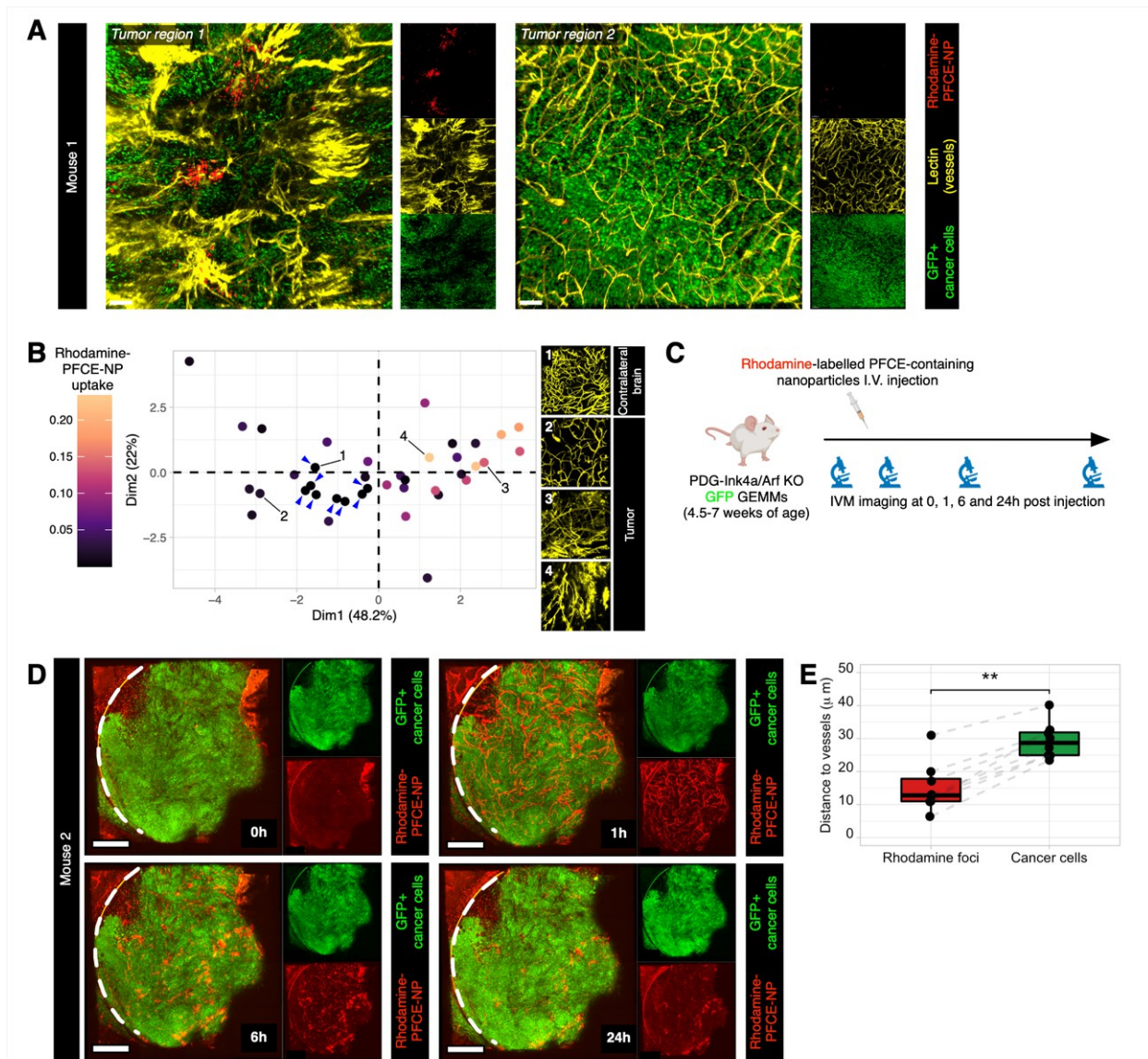


Fig. 3. PFCE-NP accumulate in proximity to dysmorphic vessels. **(A)** Representative 2-photon microscopy images of brain slices showing GFP-expressing cancer cells (green), the DyLight649-lectin-labeled vasculature (yellow), and rhodamine-PFCE-NP⁺ foci (red) in two distinct areas of the same tumor. Scale bar: 100 μm **(B)** Principal component analysis (PCA) based on 9 different vessel parameters (Z-score normalized) of different volume-of-interest (VOI) (3 to 6 VOI/mouse; n=8) in different tumor areas and healthy contralateral brain adjacent to the tumor (blue arrows). The color bar shows the rhodamine-PFCE-NP uptake (total rhodamine⁺ foci volume normalized to the total VOI volume). Images 1, 2, 3 and 4 show representative VOIs of the vascular morphology in the healthy contralateral brain (1) and the tumor (2 to 4, ranked by rhodamine-PFCE-NP uptake). **(C)** Experimental design of the intravital microscopy (IVM): GFP-PDG-Ink4a/Arf KO glioma-bearing were imaged before rhodamine-PFCE-NP administration (t=0h), 1h, 6h and 24h later. **(D)** Longitudinal imaging of the same glioma-bearing mouse by 2-photon microscopy through a cranial imaging window (CIW – white dashed line). Representative images of the glioma area below the

CIW were taken at different time points before (t=0h) and after (t=1h, 6h, 24h) injection of the rhodamine-PFCE-NP, initially showing the circulation of the NP in the bloodstream (t=1h) followed by a gradual accumulation of rhodamine⁺ foci in the tumor (t=6h and 24h). Scale bar: 500 μ m. **(E)** Quantification of the average distance to the DyLight649-lectin⁺ vessels of rhodamine-PFCE-NP⁺ foci and all GFP-positive cancer cells respectively. Mouse silhouette drawing in (C) was sourced from <https://app.biorender.com/biorender-templates>. n=8 mice; ** P<0.01, paired Wilcoxon test.

Fig. 4

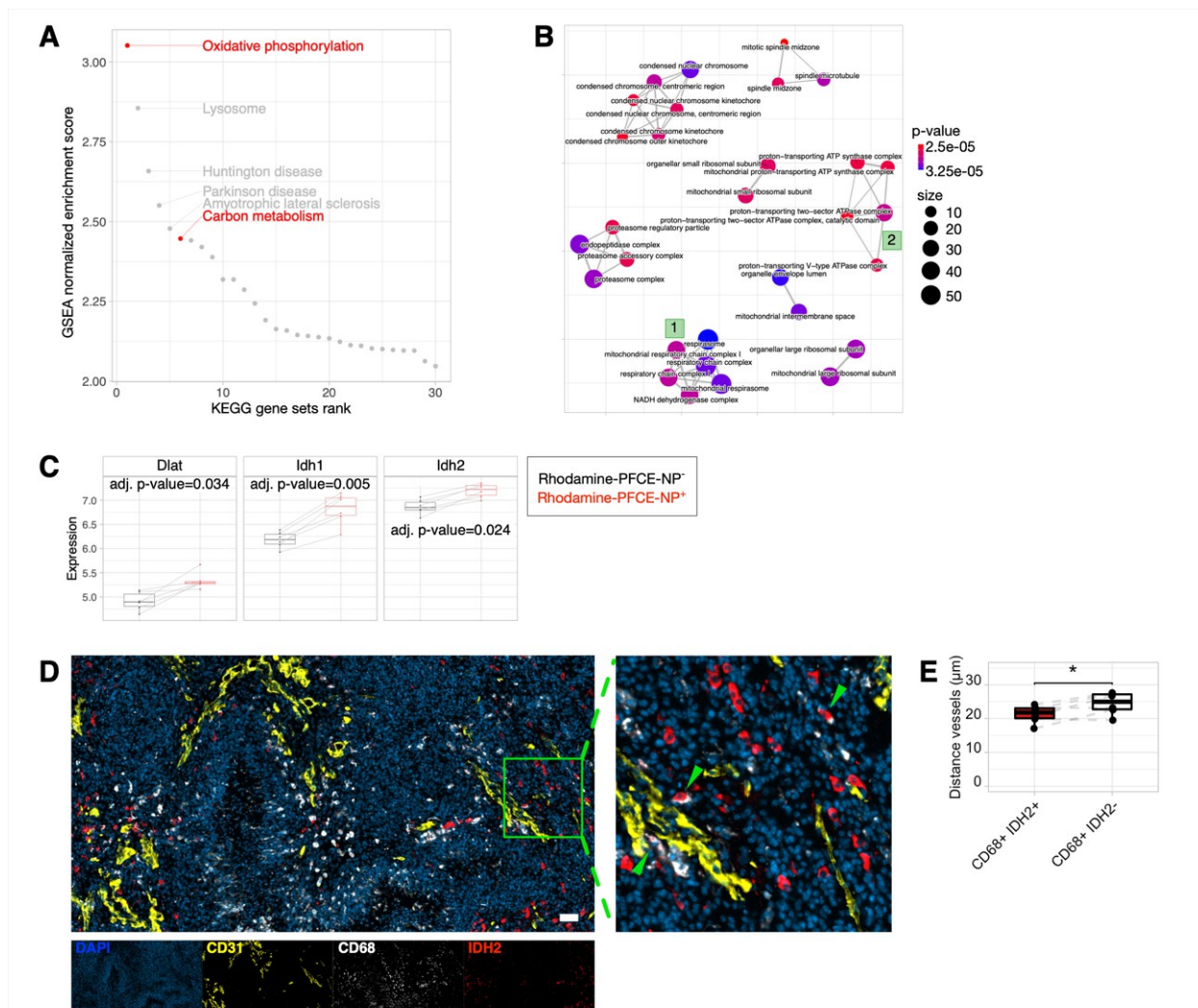


Fig. 4. PFCE-NP label a TAM subpopulation associated with high oxidative metabolic potential. **(A)** Gene-set enrichment analysis (GSEA) shows an enrichment of oxidative metabolism-related pathways in the rhodamine-PFCE-NP⁺ TAMs (KEGG pathway database). **(B)** GSEA network analysis of the top 30 enriched cellular components in the rhodamine-PFCE-NP⁺ TAMs (GO cellular component database), showing different clusters including several pathways involved in mitochondrial oxidative respiration (clusters “1” and “2” in the green squares). The dot size represents the gene set size, while the color bar indicates the p-value. **(C)** Box plots depicting normalized log₂ gene expression values for *Dlat*, *Idh1* and *Idh2* in rhodamine-PFCE-NP[±] TAMs. n=6 mice. **(D)** Representative IF staining of a PDG-Ink4a/Arf KO glioma showing DAPI⁺ cell nuclei (blue), CD68⁺ TAMs (white), IDH2⁺ cells (red), and CD31⁺ endothelial cells (yellow). The green arrows on the magnification (right) indicate CD68⁺ IDH2⁺ cells. Scale bar: 50 μm. **(E)** IF-based *Visiopharm* quantification of the distance to the vessels (CD31⁺) of CD68⁺ IDH2⁺ and CD68⁺ IDH2⁻ TAMs. n=6 mice; * P<0.05, paired Wilcoxon test.

Fig. 5

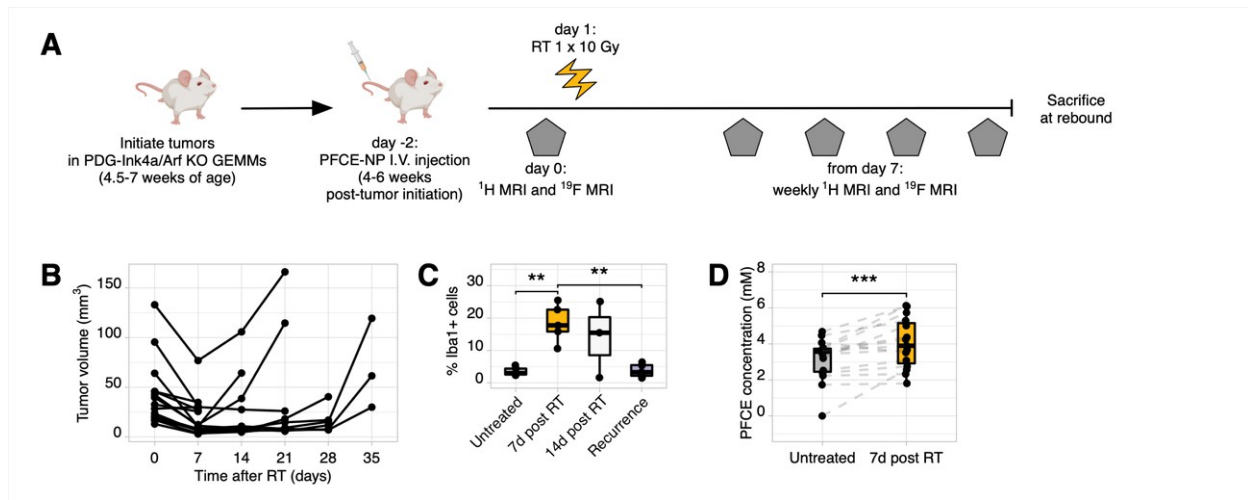


Fig. 5. The increase in TAMs following radiotherapy can be longitudinally monitored by ^{19}F MRI. **(A)** Experimental design to monitor TAM dynamics after RT by ^{19}F MRI. At tumor detection, PDG-Ink4a/Arf KO glioma-bearing mice were injected with PFCE-NP and imaged with both conventional ^1H and ^{19}F MRI to monitor tumor volume and assess the baseline ^{19}F signal. After the first ^{19}F MRI session, mice were irradiated with a single dose of 10 Gy and then imaged weekly by ^1H and ^{19}F MRI until tumor recurrence. **(B)** ^1H MRI tumor growth curves in PDG-Ink4a/Arf KO glioma-bearing mice treated with 10 Gy RT. **(C)** IF quantification of TAMs using the pan-macrophage marker Iba1, in untreated ($n=5$ mice), 7 days ($n=5$ mice), 14 days post-radiotherapy (RT) ($n=3$ mice) and recurrent ($n=7$ mice) PDG-Ink4a/Arf KO glioma tissue sections. ** $P<0.01$, unpaired Mann-Whitney test. **(D)** Quantification of the tumor PFCE concentration before and 7 days after RT ($n=15$). *** $P<0.001$, paired Wilcoxon test. Experimental trial described in (A) and (B): $n=15$ mice. Mouse silhouette drawing in (A) was sourced from <https://app.biorender.com/biorender-templates>.

Fig. 6

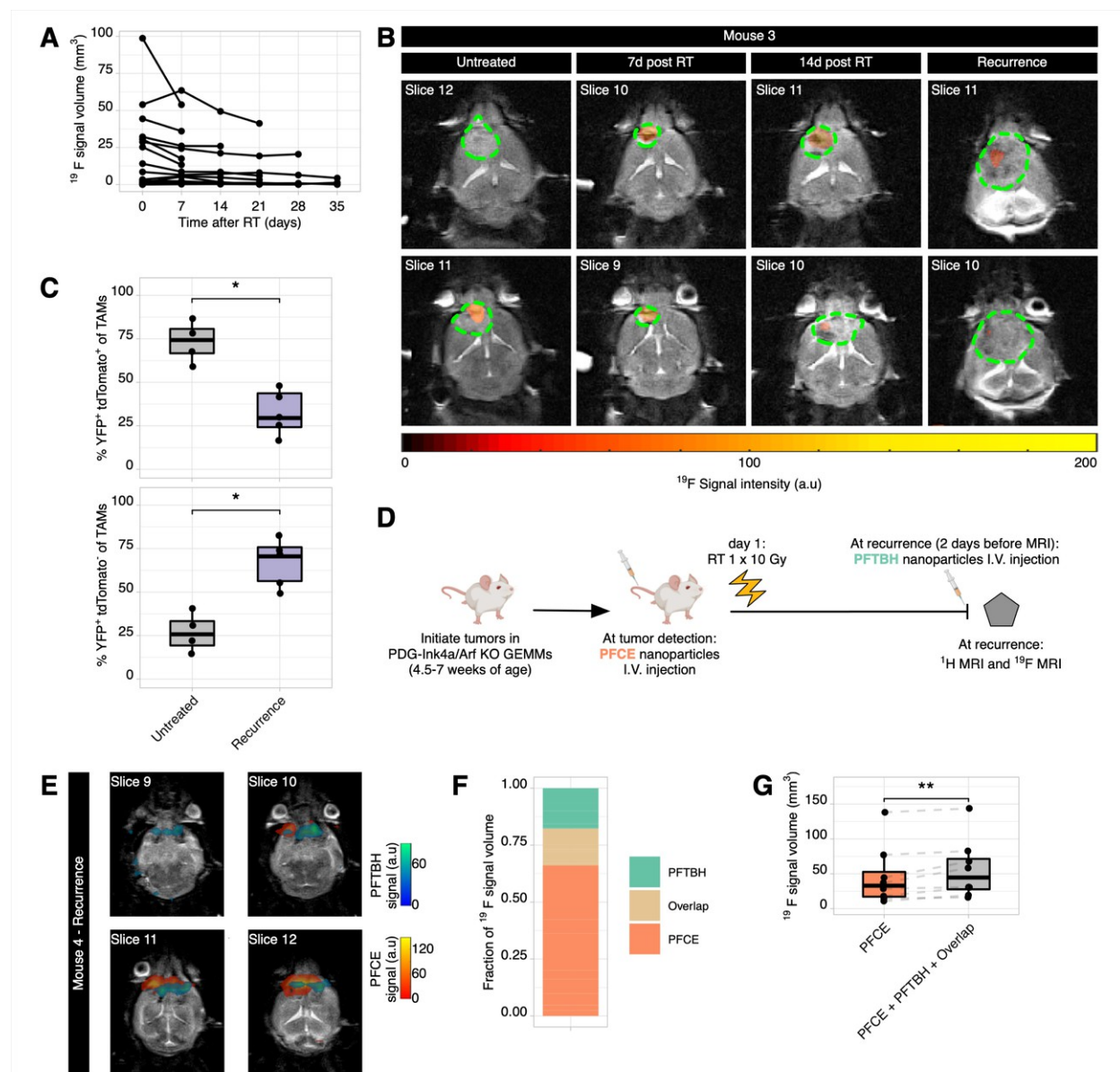


Fig. 6. Multispectral ^{19}F MRI identifies temporally-distinct niches in recurrent gliomas. **(A)** Tumor ^{19}F signal volume curves in PDG-Ink4a/Arf KO glioma-bearing mice treated with 10 Gy RT ($n=15$ mice). **(B)** Representative ^{19}F and ^1H MRI overlay images of the same mouse showing the tumor (green dashed line) and the PFCE ^{19}F signal (orange mask) over the full length of the RT trial. **(C)** IF-based quantification of MG (upper panel) and MDMs (lower panel) in untreated and recurrent glioma tissue sections. To identify MG and MDMs respectively, we used Cx3cr1:CreERT2-IRES-YFP;Rosa26:lsItdTomato mice that express tdTomato in Cx3cr1-expressing cells (MG and circulating blood monocytes) upon tamoxifen injection. Three weeks after tamoxifen-induced labeling, when blood monocytes are replenished by tdTomato $^+$ cells and only MG remain tdTomato $^+$, PDG-Ink4a/Arf KO gliomas were induced. **(D)** Experimental design to monitor TAM temporal dynamics following RT by multispectral ^{19}F MRI. Glioma bearing mice were injected with

PFCE-NP before RT and monitored weekly with conventional ^1H MRI. At detection of recurrence, mice were injected with perfluoro-tert-butylcyclohexane-containing nanoparticles (PFTBH-NP) and imaged 2 days later with ^1H and ^{19}F MRI, sequentially acquiring both PFCE and PFTBH signals. **(E)** ^1H and ^{19}F MRI overlay images of the same animal showing the distinct PFCE ^{19}F signal (red to yellow mask) and the PFTBH ^{19}F signal (blue to green mask). **(F)** Quantification of the individual compound volume fraction from the total ^{19}F signal volumes. **(G)** Quantification of the ^{19}F signal volume of PFCE only and the cumulative ^{19}F volume respectively. Mouse silhouette drawing in (D) was sourced from <https://app.biorender.com/biorender-templates>. * $P < 0.05$, ** $P < 0.01$, unpaired Mann-Whitney test in (C), and paired Wilcoxon test in (G).

Fig. 7

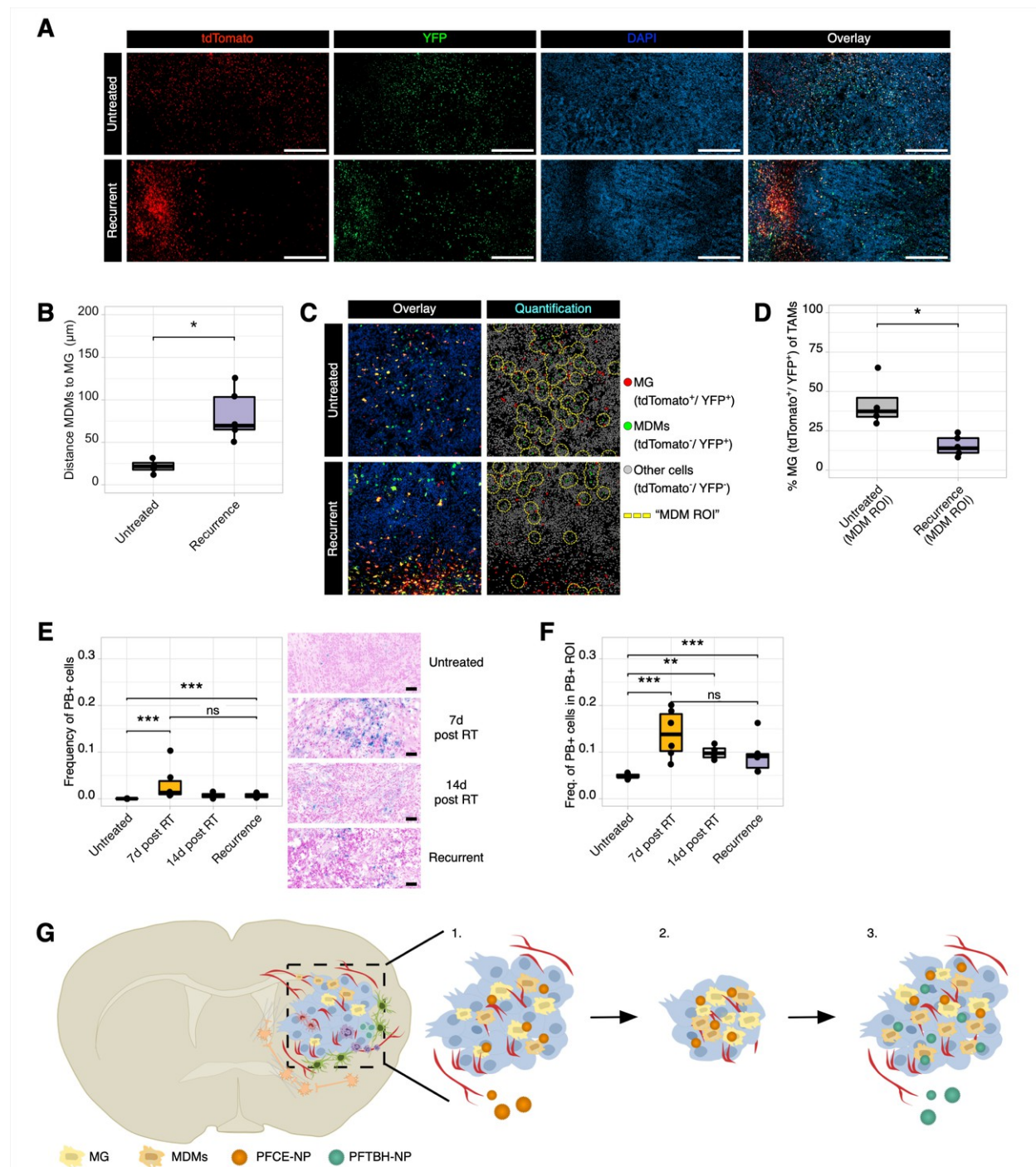


Fig. 7. MG and MDMs are differentially distributed in untreated and recurrent gliomas. **(A)** Representative IF images of the MG-specific tdTomato expression and the pan-TAM YFP expression in untreated (upper panels) and RT recurrent (lower panels) PGD-Ink4a/Arf KO gliomas in the CX3CR1 lineage tracing model. Scale bar: 500 μm. **(B)** IF-based quantification of the average distance of YFP⁺/tdTomato⁻ MDMs to

YFP+/tdTomato+ MG. **(C)** *Visiopharm* quantification pipeline showing YFP+/tdTomato+ MG (red), YFP+/tdTomato- MDMs (green) and other non-TAM YFP-/tdTomato- cells. The dashed yellow line outlines the “MDM ROI” defined around each MDM nucleus. **(D)** IF quantification of YFP+/tdTomato+ MG in the “MDM ROI” in untreated and RT-recurrent tumors. **(E)** Prussian blue (PB) staining quantification of PB+ cells in tumor tissues at different time points pre- and post-RT and corresponding representative images on the right. Scale bar: 50 μ m. **(F)** PB staining quantification of PB+ cells inside the “PB+ ROI”. **(G)** Schematic model of the cellular, spatial and temporal dynamics of TAMs and their monitoring with PFC-NP and ^{19}F MRI (illustrations were adapted from Ref. (1)). 1. PFCE-NP injection allows the specific labelling of an initial TAM population in the tumor. 2. Radiotherapy leads to tumor shrinkage, while TAMs and consequently PFCE-NP become more concentrated. 3. At tumor recurrence, the TAM subpopulations undergo a subpopulation shift and spatial changes, whereby MDMs become more abundant and distant from MG. The new spatial TAM distribution is detected by the PFTBH-NP injected at recurrence. * $P < 0.05$, *** $P < 0.001$, ns: not significant, unpaired Mann-Whitney test.